Humboldt-Universität zu Berlin

Mathematisch-Naturwissenschaftliche Fakultät

Institut für Physik

Masterarbeit

zur Erlangung des akademischen Grades Master of Science (M.Sc.)
im Fach Physik

Exploiting Symmetry in the (L)APW+LO Method

Eingereicht von:
Mara-Antonia Voiculescu

Gutachter/innen: Prof. Dr. Claudia Draxl
PD PhD Pasquale Pavone

Betreuung: Sven Lubeck

Eingereicht am Institut für Physik der Humboldt-Universität zu Berlin
am 21.02.2025

Contents

1 Introduction

Crystal symmetry plays a crucial role in understanding and predicting the properties of crystalline solids. The periodic arrangement of atoms within crystals enables their classification based on symmetry elements which, in turn, simplifies the description of their physical properties. In numerical methods, taking advantage of crystal symmetry allows for the optimization of computational techniques, improving efficiency while potentially also increasing numerical precision. In the field of computational materials science, density-functional theory (DFT) [1, 2] has become the most widely used method for studying everything from bulk crystals to surfaces, interfaces, and nanostructures. Due to its growing popularity, numerous DFT-based codes have been developed in the last decades, including the all-electron full-potential package **exciting** [3]. This code employs the (linearized) augmented planewave plus local orbitals ((L)APW+LO) method to define the basis set which is widely believed to be the gold standard of DFT, enabling calculations with exceptionally high precision [4]. However, as the size of the analyzed systems increases, so does the computational cost of this method. As such, it is particularly important to take advantage of crystal symmetry in order to achieve the best possible performance.

The goal of this thesis is the implementation of two symmetry-based methods in the **exciting** code. The first approach focuses on improving the representation of the Kohn-Sham potential by using symmetrized functions called lattice harmonics [5]. This reduces the number of terms needed to expand the potential, making it, and thus also the Hamiltonian, more efficient to compute. The second method takes advantage of inversion symmetry when solving the Kohn-Sham equations of DFT. In this case, the generally complex Hamiltonian and overlap matrices can be transformed to real ones, which simplifies the diagonalization step and significantly reduces computational cost [5]. Together, these methods considerably speed up **exciting** calculations, especially in the case of large systems.

This thesis is structured as follows: Chapter 2 introduces basic concepts of DFT, as well as the basis functions used in **exciting**. In Chap. 3, we go into detail regarding the theory behind the symmetry-based methods, while in Chap. 4, we describe their

implementation in the code. In Chap. 5, we present and evaluate the results, starting with a numerical analysis of the speedup obtained from each method individually, followed by using the combined implementation to perform calculations on perovskite barium stannate ($BaSnO_3$) [6, 7, 8], a promising material for optoelectronic applications. Finally, Chap. 6 provides a summary of our work and outlines potential future developments.

2 Theoretical Background

2.1 Density-functional theory (DFT)

The quantum-mechanical description of a solid, which consists of interacting nuclei and electrons, requires solving the many-body Schrödinger equation of the system. In practice, this is difficult to do, as a consequence of the large amount of degrees of freedom. One effective technique for reducing the complexity of this problem involves utilizing the Born-Oppenheimer approximation [9], which consists of separating the motion of the nuclei from the motion of the electrons. Within this approximation, the positions of the nuclei can be viewed as fixed, due to their significantly greater mass compared to that of the electrons. In this way, the following equation can be used to describe the electronic subsystem:

$$\hat{H}_{\mathrm{e}}\,\Psi(\mathbf{r}_1,\mathbf{r}_2,...,\mathbf{r}_N) = E\,\Psi(\mathbf{r}_1,\mathbf{r}_2,...,\mathbf{r}_N)\ , \tag{2.1}$$

where

$$\hat{H}_{\mathrm{e}} = \hat{T}_{\mathrm{e}} + \hat{V}_{\text{e-e}} + \hat{V}_{\text{e-n}}\ . \tag{2.2}$$

Here, the wavefunction $\Psi(\mathbf{r}_1,\mathbf{r}_2,...,\mathbf{r}_N)$ corresponds to a system of N electrons at positions $\mathbf{r}_j$, $\hat{T}_{\mathrm{e}}$ is the kinetic-energy operator, and the operators $\hat{V}_{\text{e-e}}$ and $\hat{V}_{\text{e-n}}$ correspond to the interaction of the electrons with each other, as well as with the nuclei, respectively.

Nonetheless, even the numerical solution of Eq. (2.1) is generally not feasible. This issue can be overcome with the help of density-functional theory (DFT), where, instead of the wavefunction, the fundamental quantity is the ground-state electron density $n(\mathbf{r})$. This method allows a significant reduction of the problem, since the electron density is a function of only three spatial coordinates, as opposed to the $3N$ coordinates of $\Psi(\mathbf{r}_1,\mathbf{r}_2,...,\mathbf{r}_N)$. In this way, the computational efforts decrease considerably, which enables the usage of DFT even for large systems.

The fundamental statement of DFT is the Hohenberg-Kohn theorem [1], according to which, for a fixed number of interacting electrons, there exists a one-to-one correspondence between the external potential, in our case $\hat{V}_{\text{e-n}} = \sum_j v_{\mathrm{ext}}(\mathbf{r}_j)$, and the ground-state electron density. As a consequence, every quantum-mechanical observable of the system can be, in principal, fully determined by the ground-state electron density. In particular,

the total ground-state energy of an interacting system of electrons is a unique functional of the electron density:

$$E[n] = F[n] + \int d\mathbf{r}\, v_{\text{ext}}(\mathbf{r})\, n(\mathbf{r}) \,, \tag{2.3}$$

where the functional $F[n]$ does not depend on the external potential. Moreover, according to Hohenberg and Kohn, the total ground-state energy functional takes its minimum at the ground-state density.

Building upon the theoretical foundation established by the Hohenberg-Kohn theorem, Kohn and Sham [2] proposed a method whose central concept is employing an auxiliary system of non-interacting particles, which has the same ground-state density as the interacting system. In this way, a single-particle scheme is constructed, which enables the calculation of the exact ground-state density and energy of the interacting electron system. Within this context, the functional $F[n]$ can be properly decomposed in the following way:

$$F[n] = T_0[n] + E_{\text{H}}[n] + E_{\text{xc}}[n], \tag{2.4}$$

where $T_0[n]$ is the kinetic energy functional of the non-interacting electron system,

$$E_{\text{H}}[n] = \frac{1}{2} \iint d\mathbf{r}_1 d\mathbf{r}_2\, \frac{n(\mathbf{r}_1)\, n(\mathbf{r}_2)}{|\mathbf{r}_1 - \mathbf{r}_2|} \tag{2.5}$$

is the Hartree energy functional, and $E_{\text{xc}}[n]$ is the exchange-correlation energy functional, which encompasses the electron-electron interactions not contained in $E_{\text{H}}[n]$, as well as the difference in kinetic energy between the interacting and non-interacting systems. After inserting this expression for $F[n]$ into Eq. (2.3), the total-energy functional can be minimized with respect to the density by constraining the particle number N. By representing the electron density using the single-particle wavefunctions of the non-interacting Kohn-Sham (KS) system[1]

$$n(\mathbf{r}) = \sum_{i,\mathbf{k}} |\psi_{i\mathbf{k}}(\mathbf{r})| \,, \tag{2.6}$$

this results in a set of single-particle equations:

$$\left[-\frac{1}{2}\nabla^2 + v_{\text{KS}}(\mathbf{r})\right] \psi_{i\mathbf{k}}(\mathbf{r}) = \epsilon_{i\mathbf{k}}\, \psi_{i\mathbf{k}}(\mathbf{r}) \,, \tag{2.7}$$

[1]The equations starting from Eq. (2.6) are already written for a periodic crystal, where the wavefunctions $\psi_{i\mathbf{k}}$ are Bloch waves of wavevector $\mathbf{k}$ and i is the band index. Here, the sum runs only over occupied states.

where

$$v_{\mathrm{KS}}(\mathbf{r},[n]) = v_{\mathrm{ext}}(\mathbf{r}) + \frac{\delta E_{\mathrm{H}}[n]}{\delta n(\mathbf{r})} + \frac{\delta E_{\mathrm{xc}}[n]}{\delta n(\mathbf{r})} = v_{\mathrm{ext}}(\mathbf{r}) + v_{\mathrm{H}}(\mathbf{r},[n]) + v_{\mathrm{xc}}(\mathbf{r},[n])\ . \tag{2.8}$$

Due to the dependency of v_{KS} on the electron density, the KS equations, Eqs. (2.6-2.8), need to be solved self-consistently. It is important to note that the KS wavefunctions and eigenvalues cannot be inherently given physical meaning, as they are only auxiliary artifacts chosen to reproduce the ground-state electron density of the real, interacting system. Nevertheless, this method is efficient in yielding the exact ground-state energy and density, provided that the exact expression for the exchange-correlation potential is known. This is, however, not the case, such that approximations need to be made for $E_{\mathrm{xc}}[n]$. Common exchange-correlation functionals include the local-density approximation (LDA) [2] and generalized-gradient approximation (GGA), such as the widely used PBE functional [10]. More advanced options, such as meta-GGA [11] and hybrid functionals [12], provide results with greater accuracy but require considerably higher computational resources.

2.2 Basis functions

2.2.1 Augmented planewaves (APWs)

Solving the KS equations within the DFT method entails choosing a basis which allows an efficient representation of the single-particle wavefunctions without losing accuracy. The augmented planewave (APW) method, developed by Slater in 1937 [13], proposes dividing the space into interstitial (I) and muffin-tin (MT) regions, in which the wavefunctions are described differently. The muffin-tins spheres of radii r_α^{MT} encompass the areas near atomic nuclei, where the potential and wavefunctions are strongly varying. Here, the wavefunctions can be described using products of spherical harmonics and solutions of the radial Schrödinger equation. Contrarily, the interstitial region between the atoms is defined by a smoother potential and wavefunctions and can thus be described efficiently using planewaves [5]. In this regard, the basis functions are defined as follows:

$$\phi_{\mathbf{G}+\mathbf{k}}(\mathbf{r}) = \begin{cases} \sum_{lm} A_{lm\alpha}^{\mathbf{G}+\mathbf{k}}\, u_{l\alpha}(r_\alpha)\, Y_{lm}(\hat{\mathbf{r}}_\alpha), & r_\alpha \le r_\alpha^{\mathrm{MT}} \\ \frac{1}{\sqrt{\Omega}}\, \mathrm{e}^{\mathrm{i}\cdot(\mathbf{G}+\mathbf{k})\cdot\mathbf{r}}, & \mathbf{r} \in I, \end{cases} \tag{2.9}$$

where $\mathbf{r}_\alpha = \mathbf{r} - \mathbf{R}_\alpha$, with $\mathbf{R}_\alpha$ being the positions of the atoms on which the muffin-tin spheres are centered. $u_{l\alpha}(r_\alpha)$ are solutions of the radial Schrödinger equation:

$$\left[-\frac{1}{2}\frac{\mathrm{d}^2}{\mathrm{d}r^2} + \frac{l(l+1)}{2r^2} + v_0(r) - \epsilon_{i\mathbf{k}}\right]\big(r\ u_{l\alpha}(r)\big) = 0\ , \tag{2.10}$$

where $\epsilon_{i\mathbf{k}}$ corresponds to an eigenvalue in Eq. (2.7). The potential $v_{\mathtt{KS}}(\mathbf{r})$ has been replaced by its spherical average $v_0(r)$ under the assumption that it is spherically symmetric due to the nearness to the nucleus [3]. $Y_{lm}(\hat{\mathbf{r}}_\alpha)$ are the complex spherical harmonics defined as:

$$Y_{lm}(\hat{\mathbf{r}}) = Y_{lm}(\theta,\varphi) = (-1)^m \sqrt{\frac{(2l+1)(l-m)!}{4\pi(l+m)!}}\ P_{lm}(\cos\theta)\ \mathrm{e}^{\mathrm{i}m\varphi}\ , \tag{2.11}$$

where θ and φ are the polar and azimuthal angles of the spherical coordinate system, respectively, and P_{lm} are the associated Legendre polynomials. The coefficients $A_{lm\alpha}^{\mathbf{G}+\mathbf{k}}$ defined in Eq. (2.9) ensure the continuity of the APWs at the sphere boundaries and can be determined as follows: Considering that the vector $\mathbf{r}_\alpha$ belongs to the sphere boundary of atom α $\big(r_\alpha = r_\alpha^{\mathtt{MT}}\big)$, the following relation holds:

$$\begin{aligned}\sum_{lm} A_{lm\alpha}^{\mathbf{G}+\mathbf{k}}\ u_{l\alpha}\big(r_\alpha^{\mathtt{MT}}\big)\ Y_{lm}(\hat{\mathbf{r}}_\alpha) &= \frac{1}{\sqrt{\Omega}}\ \mathrm{e}^{\mathrm{i}(\mathbf{G}+\mathbf{k})\cdot\mathbf{r}} = \frac{1}{\sqrt{\Omega}}\ \mathrm{e}^{\mathrm{i}(\mathbf{G}+\mathbf{k})\cdot(\mathbf{R}_\alpha+\mathbf{r}_\alpha)} \\ &= \frac{1}{\sqrt{\Omega}}\ \mathrm{e}^{\mathrm{i}(\mathbf{G}+\mathbf{k})\cdot\mathbf{R}_\alpha}\cdot\mathrm{e}^{\mathrm{i}(\mathbf{G}+\mathbf{k})\cdot\mathbf{r}_\alpha}\ .\end{aligned} \tag{2.12}$$

One can rewrite the planewave $\mathrm{e}^{\mathrm{i}(\mathbf{G}+\mathbf{k})\cdot\mathbf{r}_\alpha}$ as a spherical-harmonic expansion:

$$\mathrm{e}^{\mathrm{i}(\mathbf{G}+\mathbf{k})\cdot\mathbf{r}_\alpha} = 4\pi\ \sum_{lm} \mathrm{i}^l\ j_l\big(|\mathbf{G}+\mathbf{k}|r_\alpha^{\mathtt{MT}}\big)\ Y_{lm}^*\Big(\widehat{\mathbf{G}+\mathbf{k}}\Big)\ Y_{lm}(\hat{\mathbf{r}}_\alpha)\ , \tag{2.13}$$

where j_l are spherical Bessel functions. Substituting this expression in Eq. (2.12) leads to

$$\begin{aligned}&\sum_{lm} A_{lm\alpha}^{\mathbf{G}+\mathbf{k}}\ u_{l\alpha}\big(r_\alpha^{\mathtt{MT}}\big)\ Y_{lm}(\hat{\mathbf{r}}_\alpha) = \\ &\qquad = \frac{4\pi}{\sqrt{\Omega}}\ \mathrm{e}^{\mathrm{i}(\mathbf{G}+\mathbf{k})\mathbf{R}_\alpha}\ \sum_{lm} \mathrm{i}^l\ j_l\big(|\mathbf{G}+\mathbf{k}|r_\alpha^{\mathtt{MT}}\big)\ Y_{lm}^*\Big(\widehat{\mathbf{G}+\mathbf{k}}\Big)\ Y_{lm}(\hat{\mathbf{r}}_\alpha)\ ,\end{aligned} \tag{2.14}$$

which simplifies to

$$A_{lm\alpha}^{\mathbf{G}+\mathbf{k}}\ u_{l\alpha}\big(r_\alpha^{\mathtt{MT}}\big) = \frac{4\pi}{\sqrt{\Omega}}\ \mathrm{e}^{\mathrm{i}(\mathbf{G}+\mathbf{k})\cdot\mathbf{R}_\alpha}\ \mathrm{i}^l\ j_l\big(|\mathbf{G}+\mathbf{k}|r_\alpha^{\mathtt{MT}}\big)\ Y_{lm}^*\Big(\widehat{\mathbf{G}+\mathbf{k}}\Big)\ . \tag{2.15}$$

Following the definition of the APW basis functions, the wavefunctions can be expressed as follows:

$$\psi_{i\mathbf{k}}(\mathbf{r}) = \sum_{\mathbf{G}} C^{\mathbf{k}}_{i\mathbf{G}}\, \phi_{\mathbf{G}+\mathbf{k}}(\mathbf{r}) \;, \tag{2.16}$$

where the sum runs over the reciprocal lattice vectors $\mathbf{G}$ [3], and used to solve Eq. (2.7). By defining the elements of the Hamiltonian $\left(\underline{\underline{H}}_{\mathbf{k}}\right)$ and overlap $\left(\underline{\underline{S}}_{\mathbf{k}}\right)$ matrices in the following way

$$H^{\mathbf{GG'}}_{\mathbf{k}} = \langle \phi_{\mathbf{G}+\mathbf{k}} | \hat{h}_{\mathtt{KS}} | \phi_{\mathbf{G'}+\mathbf{k}} \rangle \;, \quad \text{with } \hat{h}_{\mathtt{KS}} = -\frac{1}{2}\nabla^2 + v_{\mathtt{KS}}(\mathbf{r}) \tag{2.17}$$

$$S^{\mathbf{GG'}}_{\mathbf{k}} = \langle \phi_{\mathbf{G}+\mathbf{k}} | \phi_{\mathbf{G'}+\mathbf{k}} \rangle \;, \tag{2.18}$$

we can transform Eq. (2.7) into a generalized eigenvalue problem:

$$\underline{\underline{H}}_{\mathbf{k}} \cdot \underline{v}_{\mathbf{k}} = \epsilon_{\mathbf{k}}\, \underline{\underline{S}}_{\mathbf{k}} \cdot \underline{v}_{\mathbf{k}} \;, \tag{2.19}$$

where the eigenvectors $\underline{v}_{\mathbf{k}}$ are formed by the coefficients defined in Eq. (2.16). However, it becomes apparent that, since the APW functions depend on $\epsilon_{i\mathbf{k}}$, Eq. (2.19) is non-linear in energy and therefore remains very complicated to solve.

2.2.2 The linearized augmented planewave (LAPW) method

One way to make Eq. (2.19) more straightforward is making it linear by choosing an energy $\epsilon_{l\alpha}$ for each l in Eq. (2.10). Nonetheless, this gives rise to other issues. For example, in practice it is difficult, or even impossible, to pick an energy parameter which is a very good approximation to the eigenenergies of all states with angular momentum l. This problem can be overcome by improving the approximation of the radial function using a Taylor expansion

$$u_{l\alpha}(r_\alpha;\epsilon) \approx u_{l\alpha}(r_\alpha;\epsilon_{l\alpha}) + (\epsilon_{l\alpha} - \epsilon)\, \dot{u}_{l\alpha}(r_\alpha;\epsilon_{l\alpha}), \tag{2.20}$$

where the derivative $\dot{u}_{l\alpha}(r_\alpha;\epsilon_{l\alpha}) = \partial u_{l\alpha}(r_\alpha;\epsilon)/\partial\epsilon$ is calculated at $\epsilon = \epsilon_{l\alpha}$. While the direct application of this expression is not feasible, it shows that the correction in the wavefunction expression has to include the energy derivative $\dot{u}_{l\alpha}(r_\alpha;\epsilon_{l\alpha})$. This gives rise to the expression for the basis functions in the muffin-tin regions within the linearized augmented planewave (LAPW) method [14, 15]:

$$\phi_{\mathbf{G}+\mathbf{k}}(\mathbf{r}) = \sum_{lm} \Big[A^{\mathbf{G}+\mathbf{k}}_{lm\alpha}\, u_{l\alpha}(r_\alpha;\epsilon_{l\alpha}) + B^{\mathbf{G}+\mathbf{k}}_{lm\alpha}\, \dot{u}_{l\alpha}(r_\alpha;\epsilon_{l\alpha}) \Big] Y_{lm}(\hat{\mathbf{r}}_\alpha), \quad r_\alpha \le r^{\mathtt{MT}}_\alpha, \tag{2.21}$$

where the coefficients $A_{lm\alpha}^{\mathbf{G}+\mathbf{k}}$ and $B_{lm\alpha}^{\mathbf{G}+\mathbf{k}}$ ensure the continuity of $\phi_{\mathbf{G}+\mathbf{k}}(\mathbf{r})$ and its spatial derivative at the sphere boundaries.

2.2.3 Local orbitals

Another approach to perform the linearization is keeping the form of the APWs defined in Eq. (2.9), but picking frozen energy parameters for the radial functions and combining them with a different kind of basis functions - local orbitals (LOs) [16]. They are defined as

$$\phi_\mu(\mathbf{r}) = \left[a_\mu \, u_{l\alpha}(r_\alpha; \epsilon_{l\alpha}) + b_\mu \, \dot{u}_{l\alpha}(r_\alpha; \epsilon_{l\alpha})\right] \, Y_{lm}(\hat{\mathbf{r}}_\alpha) \, \delta_{\alpha\alpha_\mu}\delta_{ll_\mu}\delta_{mm_\mu} \, , \tag{2.22}$$

in one specific muffin-tin and as 0 everywhere else. The coefficients a_μ and b_μ are determined by imposing that the LOs are normalized and continuous at the sphere boundary. This approach results in a smaller linearization error compared to the LAPW method, but has the minor disadvantage of increasing the number of basis functions, making it more practical for lower l-channels. If an even lower linearization error is desired, this can be achieved by taking into account higher-order energy derivatives of the radial functions. Moreover, LOs are also useful for the description of semicore states [17]. Accordingly, they can be defined with different energy parameters corresponding to the valence and semicore states.

2.3 The all-electron full-potential package `exciting`

The **`exciting`** code [3] is an all-electron full-potential DFT-based package, allowing for an accurate description of core, semicore, and valence states alike. It provides support for various methods of defining the basis set, including those mentioned above, with the added flexibility of combining them or, for instance, using different types of basis functions for different l-channels. In this thesis, we refer to this diversity using the broader term (L)APW+LO. Within this framework, the wavefunction is represented as follows:

$$\psi_{i\mathbf{k}}(\mathbf{r}) = \sum_{\mathbf{G}} C_{i\mathbf{G}}^{\mathbf{k}} \, \phi_{\mathbf{G}+\mathbf{k}}(\mathbf{r}) + \sum_{\mu} C_{i\mu}^{\mathbf{k}} \, \phi_\mu(\mathbf{r}) \, . \tag{2.23}$$

Due to the usage of two types of basis functions, the Hamiltonian matrix (as well as the overlap matrix) has the following block structure:

$$\underline{\underline{H}}_{\mathbf{k}} = \begin{pmatrix} \underline{\underline{H}}_{\mathbf{k}}^{\texttt{APW-APW}} & \underline{\underline{H}}_{\mathbf{k}}^{\texttt{APW-LO}} \\ \underline{\underline{H}}_{\mathbf{k}}^{\texttt{LO-APW}} & \underline{\underline{H}}_{\mathbf{k}}^{\texttt{LO-LO}} \end{pmatrix} . \tag{2.24}$$

The (L)APW+LO method also entails using a dual representation for physical quantities such as the charge density n or the potential $v_{\texttt{KS}}$. This consists of a planewave expansion in the interstitial region and a real-spherical-harmonic expansion inside the muffin-tin spheres:

$$f(\mathbf{r}) = \begin{cases} \sum_{lm} f_{lm}^{\alpha}(r_\alpha)\, \mathcal{S}_{lm}(\hat{\mathbf{r}}_\alpha), & r_\alpha \leq r_\alpha^{\texttt{MT}} \\ \sum_{\mathbf{G}} f_{\mathbf{G}}\, \mathrm{e}^{\mathrm{i}\mathbf{G}\cdot\mathbf{r}}, & \mathbf{r} \in I, \end{cases} \tag{2.25}$$

where $\mathbf{r}_\alpha = \mathbf{r} - \mathbf{R}_\alpha$ and f is the physical quantity being described. The real spherical harmonics $\mathcal{S}_{lm}$ are defined as:

$$\mathcal{S}_{lm} = \begin{cases} \dfrac{(-1)^m}{\sqrt{2}} \left(Y_{lm} + Y_{lm}^*\right), & m > 0, \\ Y_{l0}, & m = 0, \\ \dfrac{(-1)^m}{i\sqrt{2}} \left(Y_{l|m|} - Y_{l|m|}^*\right), & m < 0\,. \end{cases} \tag{2.26}$$

3 Symmetry-based Methods

3.1 Elements of crystal symmetry

The point group of a crystal structure is defined by the set of operations which map the crystal lattice onto itself, while leaving at least one point unmoved. In this sense, crystallographic point groups are composed of rotations, reflections, inversions, and combinations of these symmetry operations, not taking into consideration translational components. Due to constraints introduced by the periodicity of crystal lattices, 32 different crystallographic point groups can be defined. Furthermore, the site-symmetry group refers to the symmetry operations which leave a certain atomic position unchanged and is a subgroup of the crystallographic point group. The full symmetry of a crystal structure is described by the crystallographic space group, which combines the point group symmetry with the translational symmetry of the unit cell. Taking into consideration all possible combinations of these symmetry operations gives rise to a total of 230 distinct space groups [18].

The invariance of the crystal lattice under the operations of the aforementioned symmetry groups suggests that the value of certain physical quantities, such as the charge density and the potential, must be related at points connected by symmetry. In this sense, symmetrized basis functions can be defined to simplify the description of these quantities. In the interstitial region, symmetry-related planewaves can be grouped into so-called "stars", while in the muffin-tin spheres, symmetrized spherical harmonics, also called lattice harmonics, can be formed. This allows the amount of expansion coefficients to be reduced by rewriting the expansions defined in Eq. (2.25) based on these new functions. Another aspect which can be exploited is the presence of inversion symmetry. In this case, the Hamiltonian and overlap matrices can be transformed into real symmetric matrices, making their construction and diagonalization more efficient than for the complex Hermitian case that arises otherwise. The following subsections describe the theory behind these symmetry-based methods in detail, while the impact on the computational performance is discussed in Chap. 5.

3.2 Interstitial symmetrization: Stars

In the interstitial region, symmetry-adapted expansions of physical quantities can be formed by using symmetrized planewaves, known as stars, which are constructed using space group operations

$$\{\boldsymbol{\mathcal{R}}|\mathbf{t}\}\,\mathbf{r} = \boldsymbol{\mathcal{R}}\,\mathbf{r} + \mathbf{t}\ , \tag{3.1}$$

where $\boldsymbol{\mathcal{R}}$ are the rotational (or linear) parts and $\mathbf{t}$ are the translational parts of the space group [19]. The stars are defined as

$$\Phi_s(\mathbf{r}) = \frac{1}{N_{\text{op}}} \sum_{\{\boldsymbol{\mathcal{R}}|\mathbf{t}\}} \mathrm{e}^{\mathrm{i}\boldsymbol{\mathcal{R}}\mathbf{G}_s\cdot(\mathbf{r}-\mathbf{t})}\ , \tag{3.2}$$

by applying all N_{op} space group operations to a representative reciprocal lattice vector $\mathbf{G}_s$ [5]. Here, we consider the Cartesian representation of the operations $\{\boldsymbol{\mathcal{R}}|\mathbf{t}\}$. Since for symmetric lattices the same $\mathbf{G}$-vectors will be reproduced several times, a simplified form can be chosen which only sums over equal planewaves once:

$$\Phi_s(\mathbf{r}) = \frac{1}{m_s} \sum_{\mathbf{G}:\mathbf{G}=\boldsymbol{\mathcal{R}}\mathbf{G}_s} \phi_{\mathbf{G}}\, \mathrm{e}^{\mathrm{i}\mathbf{G}\cdot\mathbf{r}}\ . \tag{3.3}$$

Here, m_s is the number of distinct planewaves the star is composed of, and the phase factors $\phi_{\mathbf{G}}$ account for the presence of multiple space group operations mapping the representative vector onto the same reciprocal lattice vector $\mathbf{G}$:

$$\phi_{\mathbf{G}} = \frac{m_s}{N_{\text{op}}} \sum_{\{\boldsymbol{\mathcal{R}}|\mathbf{t}\}:\boldsymbol{\mathcal{R}}\mathbf{G}_s=\mathbf{G}} \mathrm{e}^{-\mathrm{i}\mathbf{G}\cdot\mathbf{t}}\ . \tag{3.4}$$

3.3 Muffin-tin symmetrization: Lattice harmonics

Inside the muffin-tin spheres, the symmetry of the analyzed systems can be exploited by expanding physical quantities in terms of lattice harmonics [5]. These functions are defined as linear combinations of real spherical harmonics:

$$K_\nu^\alpha(\hat{\mathbf{r}}_\alpha) = \sum_{m=-l_\nu}^{l_\nu} \Omega_{m\nu}^\alpha\, \mathcal{S}_{l_\nu m}(\hat{\mathbf{r}}_\alpha)\ . \tag{3.5}$$

Since spherical harmonics have the coordinate origin referenced to the center of an atomic site, only symmetry operations that leave the atomic position unchanged will be taken into consideration. For this reason, the coefficients $\Omega_{m\nu}^\alpha$ are determined by imposing that the lattice harmonics are invariant under all the operations of the site-symmetry group of a given atom, as opposed to the full space group. Since site symmetry operations do

not mix coefficients of spherical harmonics with different l values, only the sum over m is performed [5]. As a consequence of the rearrangement theorem, the sum over all elements in the site-symmetry group is invariant under the action of any group element [20]. For this reason, the lattice-harmonic coefficients can be determined by applying the sum over all the operations in the local site-symmetry group to the real spherical harmonics.

Applying a symmetry operation $\boldsymbol{\mathcal{R}}$ to complex spherical harmonics can be performed in the following way:

$$Y_{lm}(\hat{\mathbf{r}}') = \sum_{m'=-l}^{l} D^{l}_{m'm}(\boldsymbol{\mathcal{R}})\, Y_{lm'}(\hat{\mathbf{r}})\ , \tag{3.6}$$

where the matrix $\underline{\underline{D}}^{l}(\boldsymbol{\mathcal{R}})$ is defined as:

$$\underline{\underline{D}}^{l}(\boldsymbol{\mathcal{R}}) = (-1)^{l}\, \det(\boldsymbol{\mathcal{R}})\, \underline{\underline{D}}^{l}(\alpha,\beta,\gamma)\,. \tag{3.7}$$

Here, α, β and γ denote the Euler angles and $\det(\boldsymbol{\mathcal{R}})$ is the determinant of the matrix corresponding to the operation $\boldsymbol{\mathcal{R}}$ in the Cartesian representation. The Wigner D-matrix $\underline{\underline{D}}^{l}(\alpha,\beta,\gamma)$ is a representation of the rotation group SO(3) in the basis of spherical harmonics. Its elements are defined as [21, 22]:

$$D^{l}_{mm'}(\alpha,\beta,\gamma) = e^{-im\alpha}\, d^{l}_{mm'}(\beta)\, e^{-im'\gamma}\,, \tag{3.8}$$

with

$$\begin{aligned} d^{l}_{mm'}(\beta) = \sum_{t} (-1)^{t}\, & \frac{[(l+m)!(l-m)!(l+m')!(l-m')!]^{1/2}}{(l+m-t)!(l-m'-t)!t!(t+m'-m)!} \\ & \times \cos^{2l+m-m'-2t}(\beta/2)\, \sin^{2t+m'-m}(\beta/2). \end{aligned} \tag{3.9}$$

In order to construct a rotation matrix for real spherical harmonics, it is useful to rewrite Eq. (2.26) using matrix notation:

$$\mathcal{S}_{lm} = \sum_{m'=-l}^{l} A^{l}_{mm'}\, Y_{lm'}\ , \tag{3.10}$$

where $A^l_{m,m'}$ are elements of the matrix

$$\underline{\underline{A}}^l = \frac{1}{\sqrt{2}} \begin{pmatrix} i & 0 & \cdots & 0 & \cdots & 0 & -i(-1)^l \\ 0 & i & \cdots & 0 & \cdots & -i(-1)^{l-1} & 0 \\ \vdots & \vdots & \ddots & \vdots & \iddots & \vdots & \vdots \\ 0 & 0 & \cdots & \sqrt{2} & \cdots & 0 & 0 \\ \vdots & \vdots & \iddots & \vdots & \ddots & \vdots & \vdots \\ 0 & 1 & \cdots & 0 & \cdots & (-1)^{l-1} & 0 \\ 1 & 0 & \cdots & 0 & \cdots & 0 & (-1)^l \end{pmatrix} . \tag{3.11}$$

Based on this, the matrix $\underline{\underline{D}}^l(\boldsymbol{\mathcal{R}})$ can be transformed as follows:

$$\underline{\underline{\Delta}}^l(\boldsymbol{\mathcal{R}}) = \underline{\underline{A}}^l \cdot \underline{\underline{D}}^l(\boldsymbol{\mathcal{R}}) \cdot \left(\underline{\underline{A}}^l\right)^{-1} . \tag{3.12}$$

Subsequently, the coefficients are determined by summing over all elements of the site-symmetry group

$$\Omega^l_{m'm} = \sum_{\boldsymbol{\mathcal{R}}} \Delta^l_{m'm}(\boldsymbol{\mathcal{R}}) . \tag{3.13}$$

Finally, the coefficients are orthonormalized and those, which are linearly dependent or have zero norm, are discarded. The remaining vectors form the set of lattice-harmonic coefficients $\Omega_{m\nu}$.

3.4 Exploiting inversion symmetry

This section examines how the presence of inversion symmetry can be used to simplify the solution of the generalized eigenvalue problem defined in Eq. (2.19). In the interstitial region, the APW functions transform under the inversion operation ($\mathbf{r} \to -\mathbf{r}$) in the following way:

$$\phi_{\mathbf{G}+\mathbf{k}}(-\mathbf{r}) = \frac{1}{\sqrt{\Omega}}\, \mathrm{e}^{-\mathrm{i}(\mathbf{G}+\mathbf{k})\cdot\mathbf{r}} = \left[\frac{1}{\sqrt{\Omega}}\, \mathrm{e}^{\mathrm{i}(\mathbf{G}+\mathbf{k})\cdot\mathbf{r}}\right]^* = \phi^*_{\mathbf{G}+\mathbf{k}}(\mathbf{r})\ . \tag{3.14}$$

In systems which possess inversion symmetry, for each atom at position $\mathbf{r}$ there exists an equivalent atom at position $-\mathbf{r}$. In a MT sphere that corresponds to atom α, an APW function at position $\mathbf{r}$ has the form

$$\begin{aligned}\phi_{\mathbf{G}+\mathbf{k}}(\mathbf{r}) &= \sum_{lm} A^{\mathbf{G}+\mathbf{k}}_{lm\alpha}\, u_{l\alpha}(r_\alpha)\, Y_{lm}(\hat{\mathbf{r}}_\alpha) \\ &= \frac{4\pi}{\sqrt{\Omega}}\, \mathrm{e}^{\mathrm{i}(\mathbf{G}+\mathbf{k})\mathbf{R}_\alpha} \sum_{lm} \mathrm{i}^l\, j_l\big(|\mathbf{G}+\mathbf{k}|r^{\mathtt{MT}}_\alpha\big)\, \frac{u_{l\alpha}(r_\alpha)}{u_{l\alpha}(r^{\mathtt{MT}}_\alpha)}\, Y^*_{lm}\Big(\widehat{\mathbf{G}+\mathbf{k}}\Big)\, Y_{lm}(\hat{\mathbf{r}}_\alpha)\ ,\end{aligned} \tag{3.15}$$

as defined in Eq. (2.9). The vector $-\mathbf{r}$ lies in the opposite muffin-tin sphere, which corresponds to an atom we call β. Here, the APW basis function is defined as

$$\begin{aligned}&\phi_{\mathbf{G}+\mathbf{k}}(-\mathbf{r}) = \\ &\quad= \frac{4\pi}{\sqrt{\Omega}}\, \mathrm{e}^{\mathrm{i}(\mathbf{G}+\mathbf{k})\cdot\mathbf{R}_\beta} \sum_{lm} \mathrm{i}^l\, j_l\big(|\mathbf{G}+\mathbf{k}|r^{\mathtt{MT}}_\beta\big)\, \frac{u_{l\beta}(r_\beta)}{u_{l\beta}(r^{\mathtt{MT}}_\beta)}\, Y^*_{lm}\Big(\widehat{\mathbf{G}+\mathbf{k}}\Big)\, Y_{lm}(\hat{\mathbf{r}}_\beta)\ .\end{aligned} \tag{3.16}$$

The presence of inversion symmetry leads to the relations $\mathbf{R}_\beta = -\mathbf{R}_\alpha$ and $\mathbf{r}_\beta = -\mathbf{r}_\alpha$ between the position vectors. Together with the equality of the radial functions for symmetry-equivalent atoms, this yields:

$$\begin{aligned}&\phi_{\mathbf{G}+\mathbf{k}}(-\mathbf{r}) = \\ &\quad= \frac{4\pi}{\sqrt{\Omega}}\, \mathrm{e}^{-\mathrm{i}(\mathbf{G}+\mathbf{k})\cdot\mathbf{R}_\alpha} \sum_{lm} \mathrm{i}^l\, j_l\big(|\mathbf{G}+\mathbf{k}|r^{\mathtt{MT}}_\alpha\big)\, \frac{u_{l\alpha}(r_\alpha)}{u_{l\alpha}(r^{\mathtt{MT}}_\alpha)}\, Y^*_{lm}\Big(\widehat{\mathbf{G}+\mathbf{k}}\Big)\, Y_{lm}(-\hat{\mathbf{r}}_\alpha)\ .\end{aligned} \tag{3.17}$$

Using the property of spherical harmonics $Y_{lm}(-\mathbf{r}) = (-1)^l\, Y_{lm}(\mathbf{r})$ leads to

$$\begin{aligned}&\phi_{\mathbf{G}+\mathbf{k}}(-\mathbf{r}) = \\ &\quad= \frac{4\pi}{\sqrt{\Omega}}\, \mathrm{e}^{-\mathrm{i}(\mathbf{G}+\mathbf{k})\cdot\mathbf{R}_\alpha} \sum_{lm} (-\mathrm{i})^l\, j_l\big(|\mathbf{G}+\mathbf{k}|r^{\mathtt{MT}}_\alpha\big)\, \frac{u_{l\alpha}(r_\alpha)}{u_{l\alpha}(r^{\mathtt{MT}}_\alpha)}\, Y^*_{lm}\Big(\widehat{\mathbf{G}+\mathbf{k}}\Big)\, Y_{lm}(\hat{\mathbf{r}}_\alpha)\ .\end{aligned} \tag{3.18}$$

Making use of $Y^*_{lm}(\mathbf{r}) = (-1)^m\, Y_{l-m}(\mathbf{r})$ and substituting $m' = -m$ results in the following expression

$$\begin{aligned}\phi_{\mathbf{G}+\mathbf{k}}(-\mathbf{r}) &= \\ &= \frac{4\pi}{\sqrt{\Omega}}\, \mathrm{e}^{-\mathrm{i}(\mathbf{G}+\mathbf{k})\cdot\mathbf{R}_\alpha} \sum_{lm'} (-\mathrm{i})^l\; j_l\big(|\mathbf{G}+\mathbf{k}|r_\alpha^{\mathtt{MT}}\big)\, \frac{u_{l\alpha}(r_\alpha)}{u_{l\alpha}(r_\alpha^{\mathtt{MT}})}\; Y_{lm'}\Big(\widehat{\mathbf{G}+\mathbf{k}}\Big)\; Y^*_{lm'}(\hat{\mathbf{r}}_\alpha)\;,\end{aligned} \tag{3.19}$$

which is evidently the complex conjugate of the APW function defined in terms of vector $\mathbf{r}$, in Eq. (3.15). Thus, we have proved that in systems with inversion symmetry, the APW functions transform according to

$$\phi_{\mathbf{G}+\mathbf{k}}(-\mathbf{r}) = \phi^*_{\mathbf{G}+\mathbf{k}}(\mathbf{r})\;. \tag{3.20}$$

This property also holds for the LAPW basis functions defined in Eq. (2.21).

In the following, we analyze the impact of this aspect on the Hamiltonian matrix. By writing the matrix elements as

$$H_{\mathbf{k}}^{\mathbf{G}'\mathbf{G}} = \int \phi^*_{\mathbf{G}'+\mathbf{k}}(\mathbf{r})\, \hat{h}_{\mathtt{KS}}(\mathbf{r})\, \phi_{\mathbf{G}+\mathbf{k}}(\mathbf{r})\, d^3r\;, \tag{3.21}$$

both terms relating to basis functions can be rewritten using Eq. (3.20) :

$$H_{\mathbf{k}}^{\mathbf{G}'\mathbf{G}} = \int \phi_{\mathbf{G}'+\mathbf{k}}(-\mathbf{r})\, \hat{h}_{\mathtt{KS}}(\mathbf{r})\, \phi^*_{\mathbf{G}+\mathbf{k}}(-\mathbf{r})\, d^3r\;. \tag{3.22}$$

Substituting $\mathbf{r}' \equiv -\mathbf{r}$ yields:

$$H_{\mathbf{k}}^{\mathbf{G}'\mathbf{G}} = \int \phi_{\mathbf{G}'+\mathbf{k}}(\mathbf{r}')\, \hat{h}_{\mathtt{KS}}(\mathbf{r}')\, \phi^*_{\mathbf{G}+\mathbf{k}}(\mathbf{r}')\, d^3r'\;, \tag{3.23}$$

where we used the fact that the Hamiltonian operator is invariant under inversion, *i.e.*, $\hat{h}_{\mathtt{KS}}(-\mathbf{r}) = \hat{h}_{\mathtt{KS}}(\mathbf{r})$. Furthermore, the Hamiltonian operator is real, $\hat{h}_{\mathtt{KS}}(\mathbf{r}) = \Big[\hat{h}_{\mathtt{KS}}(\mathbf{r})\Big]^*$, which results in:

$$\begin{aligned}H_{\mathbf{k}}^{\mathbf{G}'\mathbf{G}} &= \int \phi_{\mathbf{G}'+\mathbf{k}}(\mathbf{r}')\, \Big[\hat{h}_{\mathtt{KS}}(\mathbf{r}')\Big]^*\, \phi^*_{\mathbf{G}+\mathbf{k}}(\mathbf{r}')\, d^3r' \\ &= \Big[H_{\mathbf{k}}^{\mathbf{G}'\mathbf{G}}\Big]^*\,.\end{aligned} \tag{3.24}$$

This proves that, in systems with inversion symmetry, the Hamiltonian matrix becomes real symmetric instead of complex hermitian, which can also be shown for the overlap matrix. This aspect considerably simplifies the solution of the generalized eigenvalue problem defined in Eq. (2.19).

However, LOs generally do not exhibit property (3.20). For this reason, a modification must be made in order exploit inversion symmetry in this case as well. This is done by attaching the LOs to so-called fictitious planewaves [5, 23]. By forming linear combinations,

$$\chi^{\mu}_{\mathbf{G}+\mathbf{k}}(\mathbf{r}) = \sum_{\mu'} \Lambda^{\alpha lm}_{\mathbf{G}+\mathbf{k}}\, \phi_{\mu'}(\mathbf{r})\, \delta_{l l_\mu} \ , \tag{3.25}$$

and selecting, for instance,

$$\Lambda^{\alpha lm}_{\mathbf{G}+\mathbf{k}} = \mathrm{e}^{\mathrm{i}(\mathbf{G}+\mathbf{k})\mathbf{R}_\alpha}\ \mathrm{i}^l\ Y^*_{lm}\left(\widehat{\mathbf{G}+\mathbf{k}}\right) \ , \tag{3.26}$$

new basis functions are constructed, which transform like the (L)APW basis functions

$$\chi^{\mu}_{\mathbf{G}+\mathbf{k}}(-\mathbf{r}) = \left[\chi^{\mu}_{\mathbf{G}+\mathbf{k}}(\mathbf{r})\right]^* \ . \tag{3.27}$$

In Eq. (3.25), the sum runs over equivalent LOs of atoms of the same type. The reciprocal lattice vectors $\mathbf{G}$ are chosen in such a way, so that the functions $\chi^{\mu}_{\mathbf{G}+\mathbf{k}}$ are linearly independent.

4 Implementation

4.1 Lattice harmonics

This section deals with the implementation of the symmetrized functions introduced in Chap. 3 into the **exciting** code. A key point to highlight is the fact that, in the part of the code dealing with the interstitial region, the construction of the charge density and potential is already very efficient due to the usage of fast Fourier transforms. Thus, our analysis suggests that the computational speedup gained from the implementation of stars would be negligible. For this reason, we concentrate on the implementation of the lattice harmonics within the MT spheres.

For the computation of the coefficients defined in Sec. 3.3, the matrix $\underline{\underline{A}}^l$ introduced in Eq. (3.11) was constructed, and an already-existing implementation of the Wigner-D matrix was used. Defining the coefficients as shown in Eq. (3.13) allowed for computing them in an efficient manner using matrix-matrix multiplications. This was done using tools belonging to the software package LAPACK [24]. Throughout the entirety of this project, LAPACK routines were used for handling linear algebra problems and operations, ensuring an efficient implementation of the symmetry-based methods. In order to discard linearly dependent coefficient arrays, they were identified using a Householder-based QR factorization with column pivoting, an efficient approach that provides higher numerical stability compared to other methods such as the Gram-Schmidt algorithm [25].

In the context of this project, we focus on the routine of the **exciting** code which deals with the construction of the MT potential, with the aim of switching from the expansion based on real spherical harmonics, as defined in Eq. (2.25), to the new representation based on lattice harmonics, as shown below:

$$v_{\mathrm{KS}}(\mathbf{r}) = \sum_{lm} v_{lm}(r)\, \mathcal{S}_{lm}(\hat{\mathbf{r}}) = \sum_{\nu} v_{\nu}(r)\, K_{\nu}(\hat{\mathbf{r}})\ . \tag{4.1}$$

The index α, which corresponds to the atomic site, is omitted for the sake of simplicity. Inserting the definition of the lattice harmonics, shown in Eq. (3.5), into the equation above results in the following expression for the coefficients of the transformed

potential expansion:

$$v_\nu(r) = \sum_{m=-l_\nu}^{l_\nu} \Omega_{m\nu}\, v_{l_\nu m}(r)\ . \tag{4.2}$$

Within the (L)APW+LO framework, the MT-potential contribution to the Hamiltonian matrix, as defined in Eq. (2.24), maintains the same block structure. For instance, in the APW-APW part of the matrix, the matrix elements of the potential contribution depend on terms of following form:

$$\langle \varphi_\lambda^\alpha | v_{\mathtt{KS}} | \varphi_{\lambda'}^\alpha \rangle = \sum_{lm} G^{lm}_{l_\lambda, m_\lambda, l_{\lambda'}, m_{\lambda'}} \int_0^{r_\alpha^{\mathtt{MT}}} f_\lambda^{\alpha *}(r)\, v_{lm}(r)\, f_{\lambda'}^\alpha(r) r^2\, dr\ . \tag{4.3}$$

Here,

$$\varphi_\lambda^\alpha(\mathbf{r}) = f_\lambda(r)\, Y_{l_\lambda m_\lambda}(\hat{\mathbf{r}}), \tag{4.4}$$

where $f_\lambda(r)$ refers to either $u_{l\alpha}(r_\alpha)$ or $\dot{u}_{l\alpha}(r_\alpha)$ [3]. The Gaunt coefficients $G^{lm}_{l_\lambda, m_\lambda, l_{\lambda'}, m_{\lambda'}}$ are defined as:

$$G^{lm}_{l_\lambda, m_\lambda, l_{\lambda'}, m_{\lambda'}} = \int Y_{l_\lambda m_\lambda}(\hat{\mathbf{r}})\, \mathcal{S}_{lm}(\hat{\mathbf{r}})\, Y_{l_{\lambda'} m_{\lambda'}}(\hat{\mathbf{r}}) d\mathbf{r}\ . \tag{4.5}$$

Switching from real to lattice harmonics also involves transforming the Gaunt coefficients:

$$\begin{aligned} G^{\nu}_{l_\lambda, m_\lambda, l_{\lambda'}, m_{\lambda'}} &= \int Y_{l_\lambda m_\lambda}(\hat{\mathbf{r}})\, K_\nu(\hat{\mathbf{r}})\, Y_{l_{\lambda'} m_{\lambda'}}(\hat{\mathbf{r}}) d\mathbf{r} \\ &= \sum_{m=-l_\nu}^{l_\nu} \Omega_{m\nu} \int Y_{l_\lambda m_\lambda}(\hat{\mathbf{r}})\, \mathcal{S}_{l_\nu m}(\hat{\mathbf{r}})\, Y_{l_{\lambda'} m_{\lambda'}}(\hat{\mathbf{r}}) d\mathbf{r} \\ &= \sum_{m=-l_\nu}^{l_\nu} \Omega_{m\nu}\, G^{l_\nu m}_{l_\lambda, m_\lambda, l_{\lambda'}, m_{\lambda'}}\ . \end{aligned} \tag{4.6}$$

Thus, the new matrix elements take the following form:

$$\langle \varphi_\lambda^\alpha | v_{\mathtt{KS}} | \varphi_{\lambda'}^\alpha \rangle = \sum_{\nu} G^{\nu}_{l_\lambda, m_\lambda, l_{\lambda'}, m_{\lambda'}} \int_0^{r_\alpha^{\mathtt{MT}}} f_\lambda^{\alpha *}(r)\, v_\nu(r)\, f_{\lambda'}^\alpha(r) r^2\, dr\ . \tag{4.7}$$

Equations (4.2) and (4.6) show that the shift to the new representation can be made without explicitly constructing the lattice harmonics, but instead simply by multiplying existing quantities by the coefficients $\Omega_{m\nu}$. The potential contributions to the other blocks of the Hamiltonian matrix transform analogously. It becomes clear from Eq. (4.7) that the reduction in expansion terms resulting from the lattice-harmonic implementation leads to a reduced number of integrals to be performed when computing the MT potential. As will be shown in Chap. 5, this significantly contributes to the computational speedup.

4.2 Transformation of the Hamiltonian and overlap matrices

Solving the generalized eigenvalue problem defined in Eq. (2.19), represents the computationally most demanding part of the **exciting** code for large systems. However, as discussed in Sec. 3.4, the presence of inversion symmetry can be exploited to improve computational efficiency by making the Hamiltonian and overlap matrices real. In particular, the Hamiltonian matrix (2.24) can be made real by transforming it using the matrix

$$\underline{\underline{\Gamma}}_{\mathbf{k}} = \begin{pmatrix} \mathbb{1} & 0 \\ 0 & \underline{\underline{\Lambda}}_{\mathbf{k}} \end{pmatrix} \tag{4.8}$$

in the following way

$$\begin{aligned} \underline{\underline{H}}'_{\mathbf{k}} = \underline{\underline{\Gamma}}^{\dagger}_{\mathbf{k}} \cdot \underline{\underline{H}}_{\mathbf{k}} \cdot \underline{\underline{\Gamma}}_{\mathbf{k}} &= \begin{pmatrix} \mathbb{1} & 0 \\ 0 & \underline{\underline{\Lambda}}^{\dagger}_{\mathbf{k}} \end{pmatrix} \cdot \begin{pmatrix} \underline{\underline{H}}^{\texttt{APW-APW}}_{\mathbf{k}} & \underline{\underline{H}}^{\texttt{APW-LO}}_{\mathbf{k}} \\ \underline{\underline{H}}^{\texttt{LO-APW}}_{\mathbf{k}} & \underline{\underline{H}}^{\texttt{LO-LO}}_{\mathbf{k}} \end{pmatrix} \cdot \begin{pmatrix} \mathbb{1} & 0 \\ 0 & \underline{\underline{\Lambda}}_{\mathbf{k}} \end{pmatrix} \\ &= \begin{pmatrix} \underline{\underline{H}}^{\texttt{APW-APW}}_{\mathbf{k}} & \underline{\underline{H}}^{\texttt{APW-LO}}_{\mathbf{k}} \cdot \underline{\underline{\Lambda}}_{\mathbf{k}} \\ \underline{\underline{\Lambda}}^{\dagger}_{\mathbf{k}} \cdot \underline{\underline{H}}^{\texttt{LO-APW}}_{\mathbf{k}} & \underline{\underline{\Lambda}}^{\dagger}_{\mathbf{k}} \cdot \underline{\underline{H}}^{\texttt{LO-LO}}_{\mathbf{k}} \cdot \underline{\underline{\Lambda}}_{\mathbf{k}} \end{pmatrix} , \end{aligned} \tag{4.9}$$

where the matrix $\underline{\underline{\Lambda}}_{\mathbf{k}}$ is formed by the coefficients defined in expression (3.26). The overlap matrix has the same form as the Hamiltonian matrix and transforms in the same way. As previously mentioned, the reciprocal lattice vectors $\mathbf{G}$, which the coefficients are based on, are selected to ensure that the resulting LO combinations, and thus the rows of the matrix $\underline{\underline{\Lambda}}_{\mathbf{k}}$, are linearly independent. This is done by choosing one $\mathbf{G}$-vector at a time, constructing the coefficients, and checking for linear independence with respect to the previously selected rows. To achieve this, we make use of a singular-value-decomposition (SVD) algorithm, prioritizing numerical stability. Since distinct LOs correspond to different positions within the matrix, we optimize the construction of the rows by computing coefficients for the first LO of each angular momentum l of a given atomic species and copying the values for subsequent LOs of the same l. Furthermore, once the coefficient matrix is fully constructed, we ensure that it is unitary by using a Householder-based QR-factorization algorithm. This property guarantees that the transformed Hamiltonian and overlap matrices are symmetric, *i.e.*, equal to their respective transposes. This simplifies the resulting generalized eigenvalue problem, since only the upper (or lower) triangular part of the matrices needs to be considered, thus reducing the number of operations needed for diagonalization.

In the following, we analyze the relationship between the standard generalized eigenvalue problem defined in Eq. (2.19) and the new implementation using inversion symmetry. Starting from Eq. (2.19), we multiply it from the left with $\underline{\underline{\Gamma}}_{\mathbf{k}}^{\dagger}$:

$$\underline{\underline{\Gamma}}_{\mathbf{k}}^{\dagger} \cdot \underline{\underline{H}}_{\mathbf{k}} \cdot \underline{v}_{\mathbf{k}} = \epsilon_{\mathbf{k}} \, \underline{\underline{\Gamma}}_{\mathbf{k}}^{\dagger} \cdot \underline{\underline{S}}_{\mathbf{k}} \cdot \underline{v}_{\mathbf{k}} \, . \tag{4.10}$$

Subsequently, we make use of the fact that the matrix $\underline{\underline{\Gamma}}_{\mathbf{k}}$ is unitary and add the product $\underline{\underline{\Gamma}}_{\mathbf{k}} \, \underline{\underline{\Gamma}}_{\mathbf{k}}^{\dagger} = \mathbb{1}$ before the eigenvector on both sides of the equation:

$$\underbrace{\underline{\underline{\Gamma}}_{\mathbf{k}}^{\dagger} \cdot \underline{\underline{H}}_{\mathbf{k}} \cdot \underline{\underline{\Gamma}}_{\mathbf{k}}}_{\underline{\underline{H}}'_{\mathbf{k}}} \cdot \underbrace{\underline{\underline{\Gamma}}_{\mathbf{k}}^{\dagger} \cdot \underline{v}_{\mathbf{k}}}_{\underline{v}'_{\mathbf{k}}} = \epsilon_{\mathbf{k}} \, \underbrace{\underline{\underline{\Gamma}}_{\mathbf{k}}^{\dagger} \cdot \underline{\underline{S}}_{\mathbf{k}} \cdot \underline{\underline{\Gamma}}_{\mathbf{k}}}_{\underline{\underline{S}}'_{\mathbf{k}}} \cdot \underbrace{\underline{\underline{\Gamma}}_{\mathbf{k}}^{\dagger} \cdot \underline{v}_{\mathbf{k}}}_{\underline{v}'_{\mathbf{k}}} \, . \tag{4.11}$$

As shown in the expression above, we recognize the transformation of the Hamiltonian and overlap matrices as described in Eq. (4.9) and denote them by $\underline{\underline{H}}'_{\mathbf{k}}$ and $\underline{\underline{S}}'_{\mathbf{k}}$, respectively. It can be observed that the eigenvalues $\epsilon_{\mathbf{k}}$ remain unchanged, as expected from the similarity transformation of the matrices. Moreover, the eigenvectors transform according to:

$$\underline{v}_{\mathbf{k}} = \underline{\underline{\Gamma}}_{\mathbf{k}} \cdot \underline{v}'_{\mathbf{k}}. \tag{4.12}$$

This approach allows us to easily switch between the two representations. It enables us to perform the diagonalization in the real case and then back-transform the eigenvectors to ensure compatibility with the rest of the **exciting** code. The impact on computational performance is discussed in the next section.

5 Results

5.1 Speedup analysis: Lattice harmonics

In this section, we analyze the impact of the lattice harmonics defined in Sec. 3.3 onto the time required to compute the MT potential. We focus on six materials with atoms corresponding to different site-symmetry groups. Each group contains a different number of symmetry operations, as detailed in Tab. 5.1. In this analysis, we consider calculations with a maximum value of the angular momentum quantum number l equal to 12. The number of terms in the real-spherical-harmonic expansion of the potential, described in Eq. (2.25), is given by $(l_{\max} + 1)^2 = 169$. Table 5.1 also shows that different site-symmetry groups lead to different numbers of terms in the lattice-harmonic expansion, when switching to the new representation as described in Eq. (4.1).

Table 5.1: Site-symmetry group, number of symmetry operations, and number of terms in the lattice-harmonic (LH) expansion for the six analyzed materials. Expansions are performed with a maximum value of the angular momentum quantum number l equal to 12.

System	K	ZnO	CdSe	CBa	C	Mo
Site-symmetry group	m	mm2	3m	4mm	-43m	m-3m
Nr. symmetry operations	2	4	6	8	24	48
Nr. LH expansion terms	91	49	35	28	11	8

Since different site-symmetry groups can contain the same number of symmetry elements, there is no one-to-one correspondence between the number of group elements and the number of terms in the lattice-harmonic expansion. However, systems higher in symmetry generally correspond to fewer terms, leading to increased computational efficiency. Figure 5.1 illustrates the speedup obtained using the lattice-harmonic implementation to compute the MT potential for the six different structures. Here, we define the speedup as the ratio of the computation time required for the MT potential using the standard real-spherical-harmonic representation to the time needed using the new implementation. The speedup is plotted against the number of lattice harmonic expansion terms. In this sense, lower values on the x-axis correspond to higher symmetry. The results, averaged

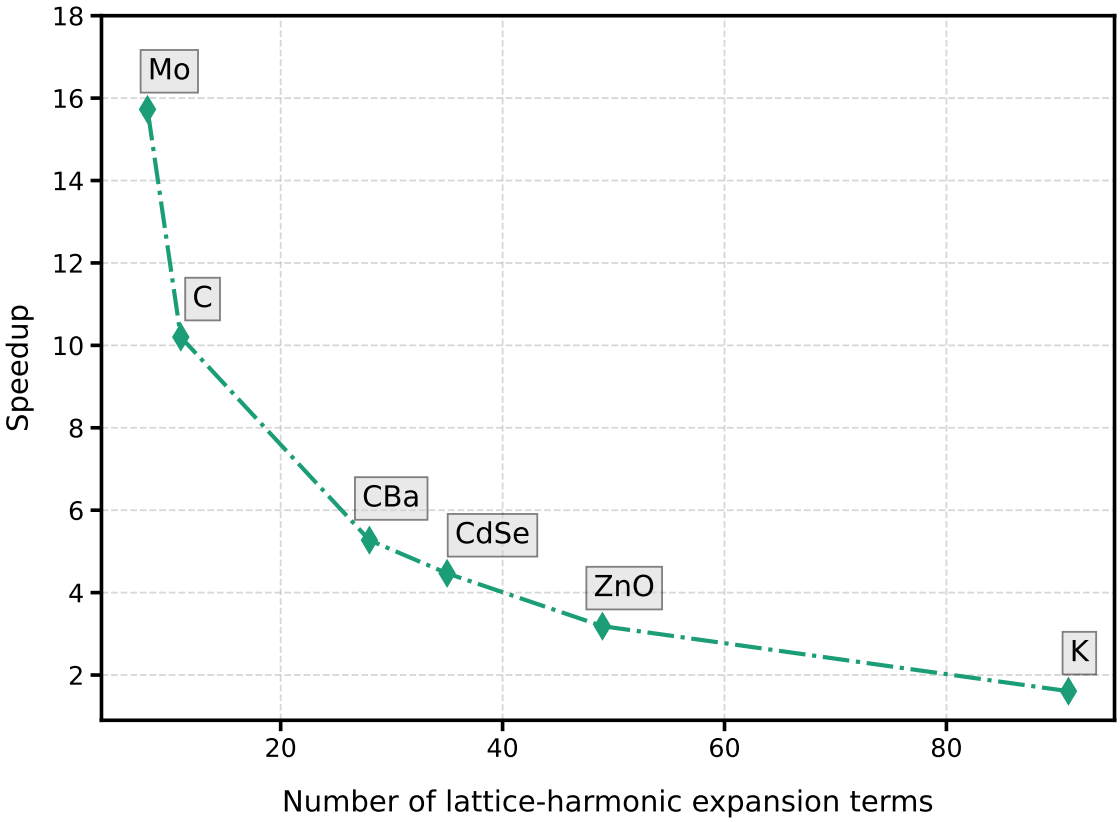

Figure 5.1: Speedup gained using the lattice-harmonic implementation to compute the MT potential for the six different materials in Tab. 5.1, obtained by using the serial version of the **exciting** code.

over six calculations per structure using serial executions of the **exciting** code, show that the computation was nearly twice as fast for the structure with the lowest symmetry and up to about sixteen times faster for the most symmetric system.

An important aspect to keep in mind in the lattice-harmonic implementation is the overhead introduced by generating the lattice-harmonic coefficients, as defined in Eq. (3.13), and transforming both the potential and Gaunt coefficients, as shown in Eqs. (4.2) and (4.6), respectively. Figure 5.2 provides an analysis of the speedup, broken down into different contributions in order to better understand the observed behavior. The data are plotted on a logarithmic scale to make the comparison easier. The lines connecting the data points are included as a guide for the eye. Since the time required to compute the MT potential is directly proportional to the number of expansion terms, we define the optimal speedup limit as the ratio of the number of real-spherical-harmonic expansion terms to the number of lattice-harmonic expansion terms. This is the maximum possible speedup and is represented by the orange solid line. The purple square data points represent the time needed only for the actual computation of the potential, excluding all overhead processes. As expected, they are in very good agreement with the orange solid line, confirming the correctness of our analysis. To examine the impact of overhead

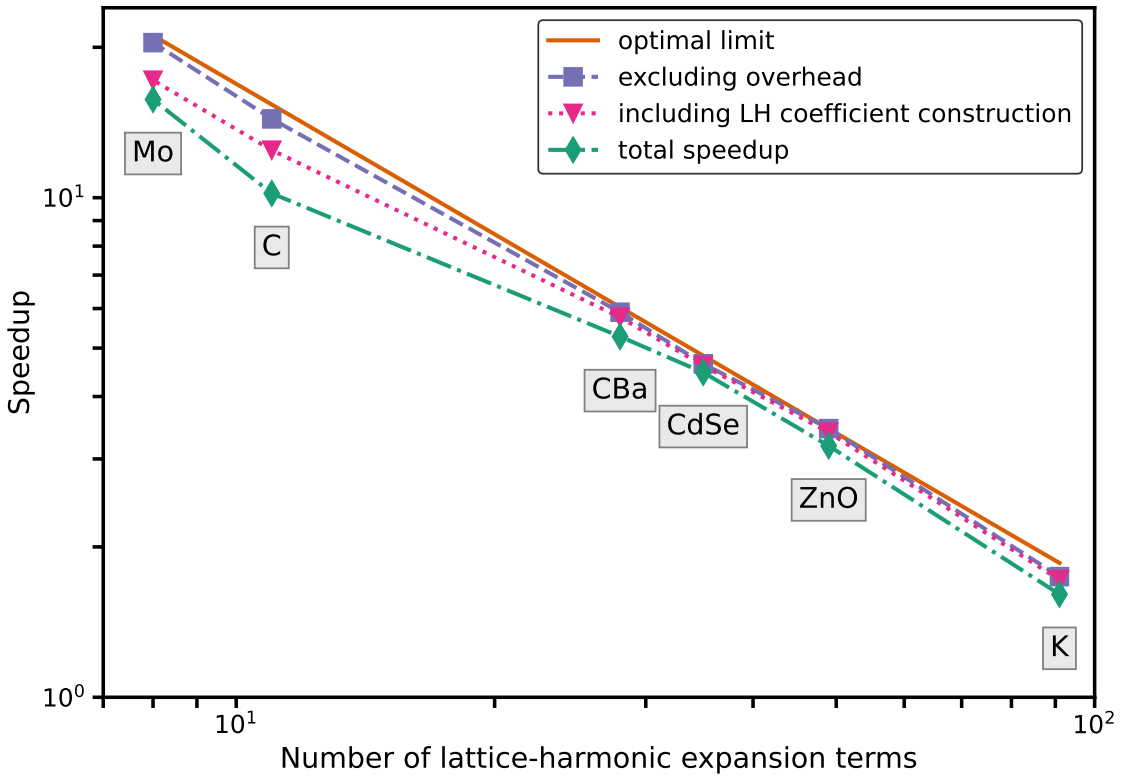

Figure 5.2: Analysis of the speedup from the lattice-harmonic implementation across the six materials, obtained from serial executions of the **exciting** code. The orange solid line represents the optimal speedup. The purple squares exclude all overhead terms, while the pink triangles include only the construction of the lattice-harmonic (LH) coefficients. The turquoise diamonds show the actual speedup, including both the LH-coefficient generation and the transformation of the potential and Gaunt coefficients.

processes, we include the construction of the lattice-harmonic coefficients in the pink triangles, while the turquoise diamonds correspond to the full implementation (shown in Fig. 5.1), including also the transformation of the potential and Gaunt coefficients. The results show that the computation of lattice-harmonic coefficients introduces a larger overhead in systems with higher symmetry due to the larger number of symmetry elements. Nevertheless, we are still able to achieve a significant speedup.

The **exciting** code is not only serially executable, but also makes use of parallelization techniques to accelerate calculations. Therefore, the next part of our analysis consists of repeating the previous calculations using parallel runs of the code with four OpenMP threads [26], as shown in Fig. 5.3. The results show higher discrepancies compared to the serial case. Since the actual computation of the MT potential is parallelized in both the old and new versions of the code, the purple and orange lines are still in close agreement. However, the significant differences observed in the pink and turquoise symbols indicate that the overhead processes could benefit from parallelization. In addition, these discrepancies suggest that the generation of the lattice-harmonic coefficients could be

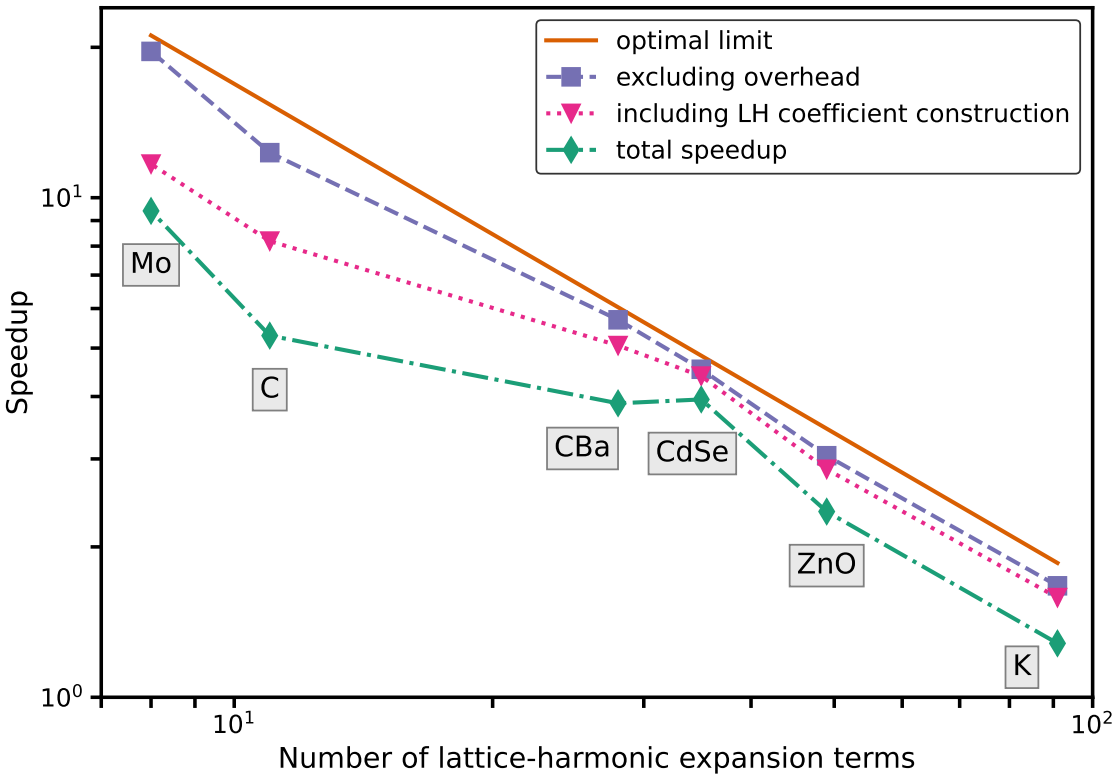

Figure 5.3: Analysis of the speedup from the lattice-harmonic implementation across the six materials, obtained from parallel executions of the **exciting** code with four OpenMP threads. The orange solid line represents the optimal speedup. The purple squares exclude all overhead terms, while the pink triangles include only the construction of the lattice-harmonic (LH) coefficients. The turquoise diamonds show the actual speedup, including both the LH-coefficient generation and the transformation of the potential and Gaunt coefficients.

further optimized. Despite the overhead, we are still able to compute the MT potential up to nearly ten times faster. Even for less symmetric systems, the overhead never offsets the performance gains from using the lattice-harmonic implementation. As a result, this method consistently outperforms the standard real-spherical-harmonic representation.

5.2 Speedup analysis: Inversion symmetry

In this section, we examine the influence of the transformation of Eq. (2.19) in the presence of inversion symmetry on the computational performance. To assess this, we perform calculations of a PtF_6 structure, varying the size of the Hamiltonian and overlap matrices by adjusting the number of (L)APW basis functions used. Throughout this analysis, the number of LOs is kept constant. Since our focus is on the numerical evaluation, we significantly relax the computational parameters and perform calculations for only one **k**-point. The results shown in this section correspond to the average timings for a single

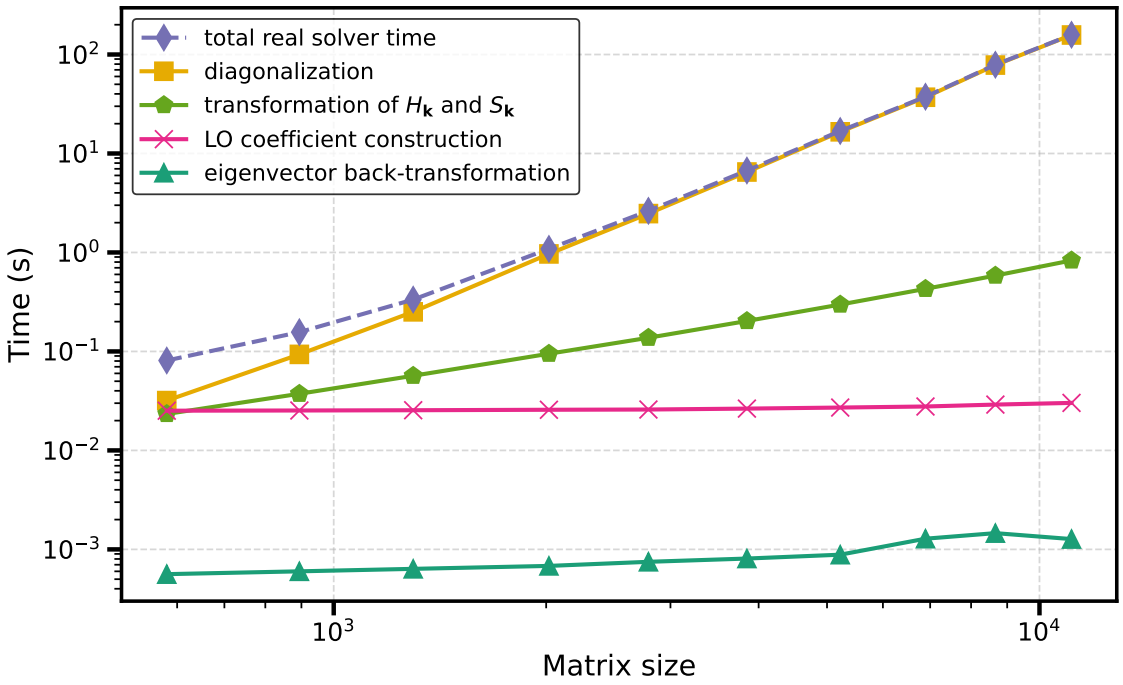

Figure 5.4: Analysis of the execution time required by the different contributions to the real solver plotted as a function of matrix size. Shown here is the time needed for diagonalization (yellow squares), Hamiltonian and overlap matrix transformation (green pentagons), LO-coefficient matrix construction (pink crosses), and eigenvector back-transformation (turquoise triangles). The sum of these contributions corresponds to the total time needed for the real solver (purple diamonds). The lines connecting the data points are included as a guide for the eye. The data are obtained from serial executions of the **`exciting`** code.

iteration of the self-consistent loop, allowing us to perform a consistent comparison across structures. Figure 5.4 contains an analysis of the time required to solve the generalized eigenvalue problem using the inversion-symmetry-based real solver (purple diamonds).

Each data point corresponds to an average over six calculations performed using serial executions of the code. Like in the case of the lattice-harmonic implementation, there are overhead terms that must be taken into consideration. These include the construction of the LO-coefficient matrix $\underline{\underline{\Lambda}}_\mathbf{k}$ described in (4.8) (pink crosses), the transformation of the Hamiltonian and overlap matrices as shown in Eq. (4.9) (green pentagons), and the inverse transformation of the eigenvectors described in Eq. (4.12) (turquoise triangles). Moreover, we plot the time required just for the diagonalization of the transformed matrices, represented by the yellow squares. In this sense, the purple diamond data points, corresponding to the real solver, are equal to the sum of the other plots. In order to facilitate the comparison of the different contributions, we represent the data on a logarithmic scale. It becomes apparent that the back-transformation of the eigenvectors is the least computationally expensive task, followed by the construction of the coefficients. As expected, the time needed to compute the $\underline{\underline{\Lambda}}_\mathbf{k}$ matrix remains fairly constant across

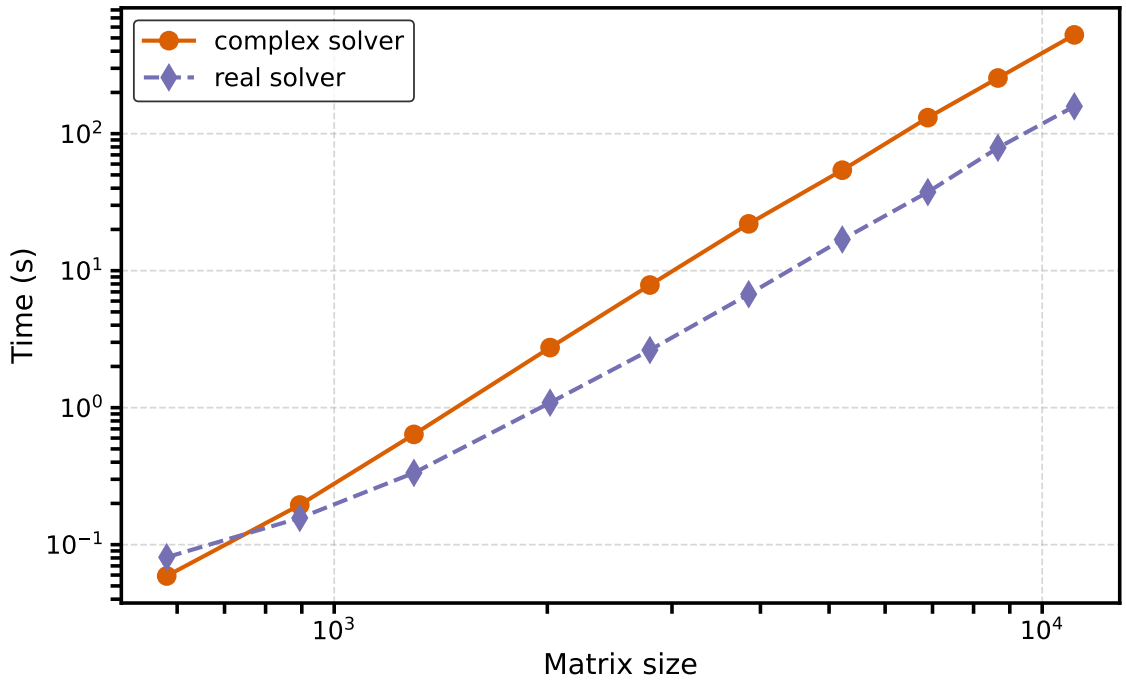

Figure 5.5: Comparison of the time needed for solving the generalized eigenvalue problem defined in Eq. (2.19) in the presence of inversion symmetry, using the standard complex solver (orange circles) and the real solver (purple diamonds) as a function of matrix size. The data was obtained from serial executions of the **`exciting`** code.

the different matrix sizes due to the fixed number of LOs used in each calculation. On the other hand, the time needed for the Hamiltonian and overlap matrix transformation increases with the matrix size. However, the most time-intensive component of the real solver is the diagonalization of the matrices, as indicated by the agreement between the yellow and purple plots.

Figure 5.5 shows a comparison of the time required to solve the standard complex eigenvalue problem (orange circles) versus the transformed real-valued problem (purple diamonds). For the smallest system, with a matrix size of 580, the construction of the coefficients and the transformation of the matrices account for a relatively large fraction of the real solver's computation time, so that this method requires more time overall than the standard complex solver. Nonetheless, for systems of this size, calculations are generally computationally cheap, making this difference negligible. For all other matrix sizes, the real solver outperforms the complex one, achieving a speedup of over 3.3 for the largest system.

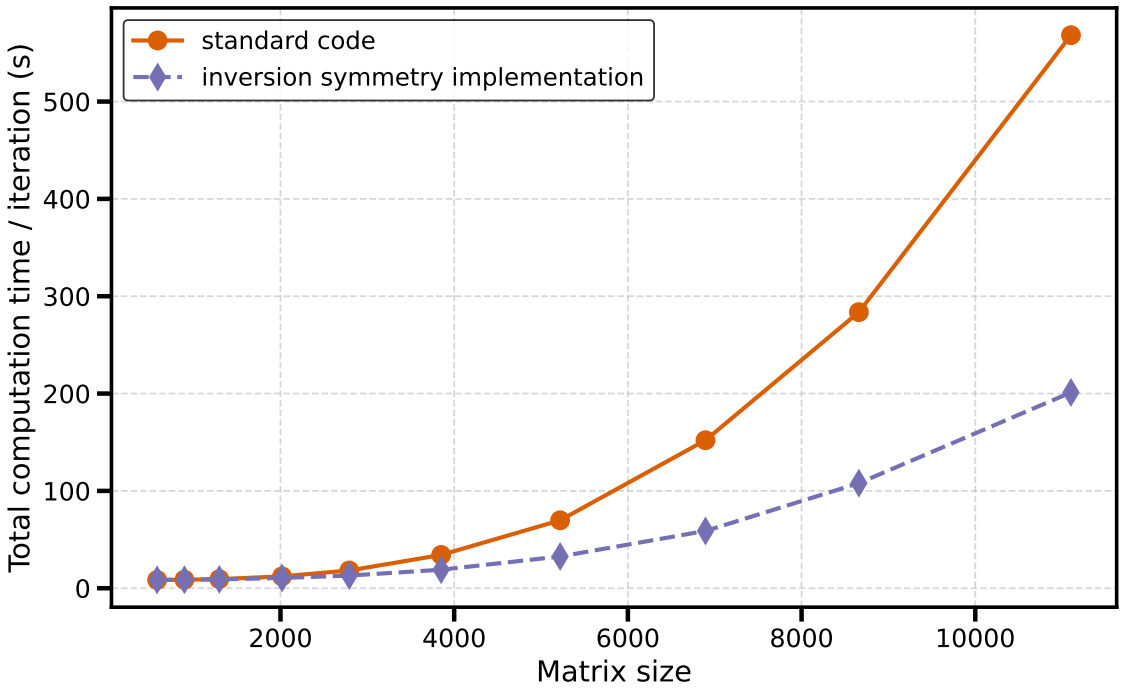

Figure 5.6: Comparison of the average total time required for an iteration of the standard **`exciting`** code (orange circles) and the code considering inversion symmetry (purple diamonds), in the case of serial calculations.

Figure 5.6 illustrates the impact of this implementation on the average time needed for an iteration of the code across matrix sizes. Since we considered the total computation time when averaging over the number of iterations, the time needed for initialization is also included in these results. As already mentioned, solving Eq. (2.19) dominates the overall computation time for large systems. Consequently, as the matrix size increases, the speedup in the total computation time approaches the speedup observed when comparing the solvers only. For the largest system, we achieve a speedup of almost three for an average iteration of the code.

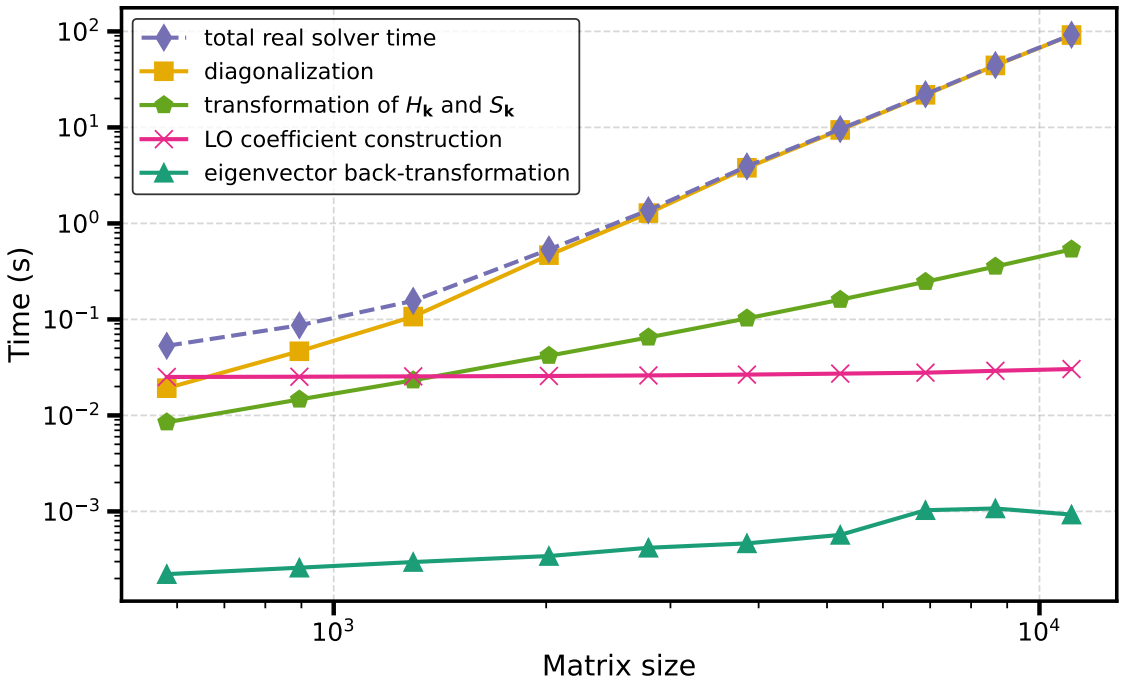

Figure 5.7: Analysis of the execution time required by the different contributions to the real solver plotted as a function of matrix size. Shown here is the time needed for diagonalization (yellow squares), Hamiltonian and overlap matrix transformation (green pentagons), LO-coefficient matrix construction (pink crosses), and eigenvector back-transformation (turquoise triangles). The sum of these contributions corresponds to the total time needed for the real solver (purple diamonds). The lines connecting the data points are included as a guide for the eye. The data was obtained from parallel executions of the **exciting** code with four OpenMP threads.

When repeating the calculations using parallel executions with four OpenMP threads, as shown in Figs. 5.7, 5.8, and 5.9, we observe that the real solver takes longer than the standard complex solver for the two smallest systems. However, this does not have a large impact on the overall computation time, as the time required for a full calculation is almost equal in both cases. For the largest system, we are able to achieve a speedup of four in the solver comparison, which corresponds to a 3.5-times-faster execution in the case of a full calculation. Our speedups in both the serial and parallel cases are in agreement with those observed for other (L)APW+LO-based codes [27, 28], which report factors ranging between three and four. In particular, the WIEN2k code achieves a speedup of almost four [27], but it is important to mention that their implementation uses a fully real version of the code, including the direct construction of real matrices rather than just their transformation. This is likely the reason for the higher speedup observed in this case.

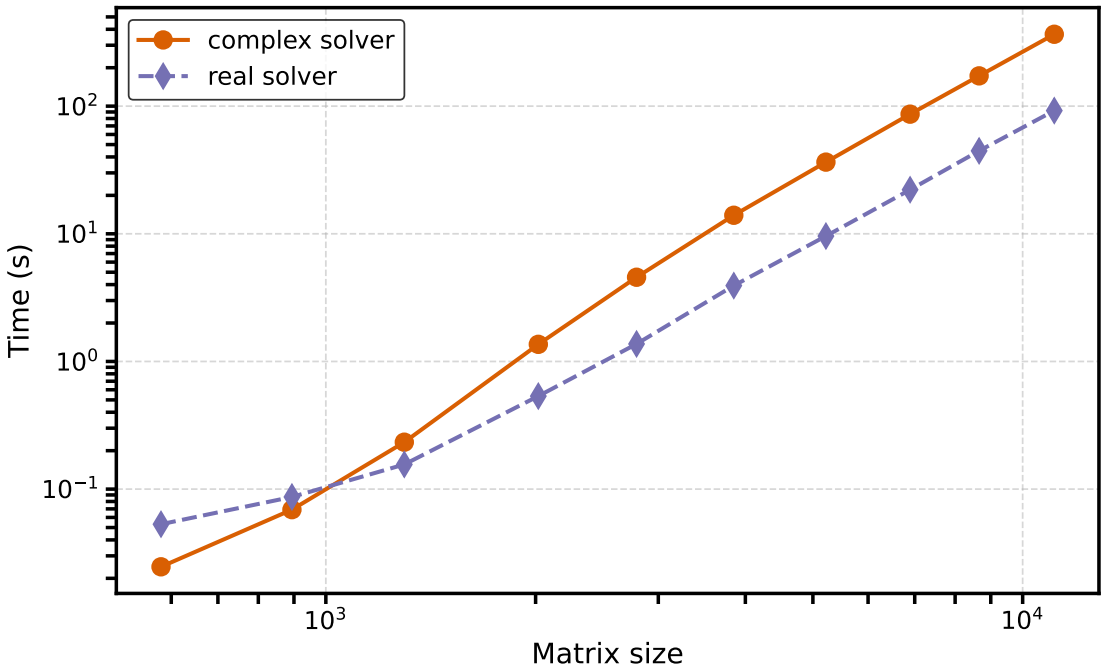

Figure 5.8: Comparison of the time needed for solving the generalized eigenvalue problem defined in Eq. (2.19) in the presence of inversion symmetry, using the standard complex solver (orange circles) and the real solver (purple diamonds) as a function of matrix size. The data was obtained from parallel executions of the **`exciting`** code with four OpenMP threads.

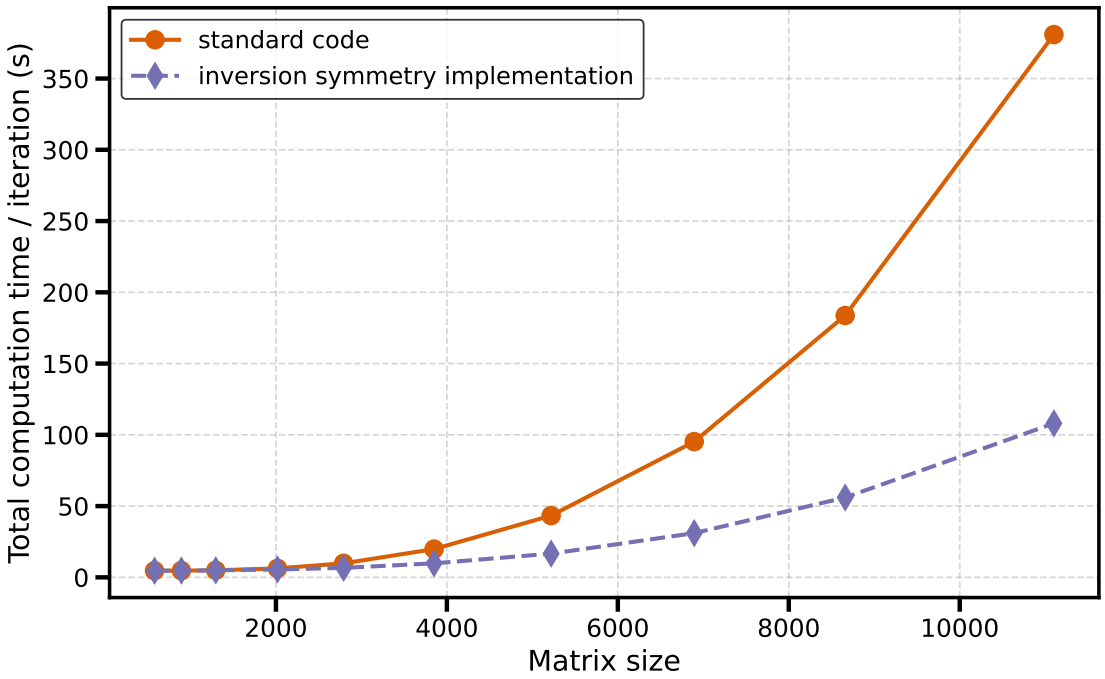

Figure 5.9: Comparison of the average total time required for an iteration of the standard **`exciting`** code (orange circles) and the code considering inversion symmetry (purple diamonds), in the case of parallel calculations with four OpenMP threads.

5.3 Example of $BaSnO_3$

Perovskite barium stannate ($BaSnO_3$) is one of the most promising emerging materials for optoelectronic devices due to its extraordinary room-temperature carrier mobility of up to 320 $cm^2\,V^{-1}\,s^{-1}$ and its high thermal stability. Because of these properties, it has become the focal point of many theoretical and experimental studies [6, 7, 8]. For example, in Ref. [8] the theoretical analysis includes the description of the electronic structure and the optical properties of $BaSnO_3$ using state-of-the-art methods based on many-body perturbation theory (MBPT), in comparison with experiment. In MBPT, DFT ground-state calculations are used as a starting point. For this reason, we study the impact of the symmetry-based methods introduced in this thesis onto the ground-state calculations of this material.

Perovskite $BaSnO_3$ is characterized by a highly-symmetric unit cell. The oxygen atoms correspond to the site-symmetry group 4/mmm, which contains 16 symmetry operations, while the site-symmetry group of the barium and tin atoms is m-3m, containing the highest possible number of 48 symmetry elements. This aspect is favorable for the lattice-harmonic implementation, while the presence of inversion symmetry allows us to employ the real solver described in the previous subsection. In Tables 5.2 and 5.3, we compare the results of the calculations performed using the standard **`exciting`** code with those obtained using the symmetry-based methods. As in the case of the speedup analyses shown in the previous sections, we consider both serial executions and parallel executions with four OpenMP threads. The calculations were performed with the PBEsol exchange-correlation functional [29] and an $8\times8\times8$ **k**-grid. The MT-sphere radii for Ba, O, and Sn were set to 1.9226, 1.513, and 1.9875 a_0, respectively. Using a maximum value of the angular momentum quantum number l equal to 12, 171 LOs and a maximum number of 1856 planewaves, corresponds to a maximum matrix size of 2027.

Table 5.2: Comparison of execution times of $BaSnO_3$ calculations obtained with the standard `exciting` code and the symmetry-based implementation. Shown here are the total computation time, the time needed to solve the generalized eigenvalue problem given by Eq. (2.19) and to compute the MT potential. The time required by the individual contributions of the symmetry-based methods are also included. The results were obtained from serial executions of the code.

CPU times [s]	**Standard code**	**Symmetry-based code**	
Total	**3203.82 s**	**1909.92 s**	
Solver	**1966.01 s**	**749.63 s**	
		diagonalization	716.38 s
		LO coefficient construction	3.85 s
		transformation of $\underline{\underline{H}}_{\mathbf{k}}$ and $\underline{\underline{S}}_{\mathbf{k}}$	28.28 s
		eigenvector back-transformation	1.12 s
MT potential	**99.76 s**	**8.48 s**	
		potential synthesis	8.10 s
		LH coefficient construction	0.12 s
		Gaunt coefficient transformation	0.21 s
		potential coefficient transformation	0.05 s

Table 5.3: Comparison of execution times for $BaSnO_3$ calculations obtained with the standard `exciting` code and the symmetry-based implementation. Shown here are the total computation time, the time needed for solving the generalized eigenvalue problem given by Eq. (2.19) and for computing the MT potential. The time required by the individual contributions of the symmetry-based methods are also included. The results were obtained from parallel executions of the code, using four OpenMP threads.

CPU times [s]	**Standard code**	**Symmetry-based code**	
Total	**1476.43 s**	**780.20 s**	
Solver	**1037.81 s**	**364.80 s**	
		diagonalization	344.92 s
		LO coefficient construction	4.13 s
		transformation of $\underline{\underline{H}}_{\mathbf{k}}$ and $\underline{\underline{S}}_{\mathbf{k}}$	15.10 s
		eigenvector back-transformation	0.65 s
MT potential	**26.29 s**	**2.69 s**	
		potential synthesis	2.30 s
		LH coefficient construction	0.12 s
		Gaunt coefficient transformation	0.21 s
		potential coefficient transformation	0.05 s

The results shown in Tables 5.2 and 5.3 are in good agreement with the speedup analyses performed in the previous sections. In the case of the serial execution of the **exciting** code, the solution of the generalized eigenvalue equation was about 2.6 times faster, while for the potential contribution we observed a speedup of almost twelve. These results correspond to an overall speedup of about 1.7. In the parallel case, the real solver was almost three times faster than the complex one, and together with an almost tenfold speedup of the potential, we achieved an overall speedup of about 1.9. These results are satisfactory considering that this system is not particularly large. Moreover, the comparison of the total ground-state energy and the estimated fundamental band gap confirms the validity of our implementation, reproducing the results of the standard code with a maximum difference of order 10^{-9} Ha for the energy and 10^{-11} Ha for the Kohn-Sham band gap.

6 Conclusion and Outlook

In summary, we have implemented two symmetry-based methods into the all-electron full-potential package **exciting**. First, symmetrized spherical harmonics, called lattice harmonics, were introduced, which allowed us to reduce the number of terms needed for the expansion of the potential. The speedup analysis included in this thesis showed that our implementation consistently outperforms the standard real-spherical-harmonic representation across the analyzed materials. In particular, for the system highest in symmetry, corresponding to the site-symmetry group m-3m, we were able to compute the MT potential nearly sixteen times faster. Second, we took advantage of inversion symmetry, which leads to a real-valued generalized eigenvalue equation, simplifying the diagonalization of the Hamiltonian and overlap matrices compared to the standard complex case. Applying this method to systems with different matrix sizes, we were able to achieve a speedup of four compared to the complex solver. Correspondingly, the total time required for an **exciting** calculation was reduced by more than 3.5. Both methods highlight the advantage of exploiting symmetry in DFT calculations within the (L)APW+LO framework, yielding a significant reduction in computational time, especially for large systems. The validity and gain of our implementation is further confirmed by the application to $BaSnO_3$.

Going forward, the usage of lattice harmonics can be explored for other quantities which are typically represented in terms of (real) spherical harmonics, such as the charge density. Moreover, the results presented in this thesis underline the benefit of introducing parallelization strategies for the construction of newly-introduced overhead terms, such as the lattice-harmonic coefficients. Regarding inversion symmetry, the most straightforward future development is to construct real Hamiltonian and overlap matrices right from the start, rather than transforming from complex to a real matrices just before the diagonalization. As part of this project, we have already laid down the groundwork for this possible implementation. Employing the LO coefficients, which allow attaching them to fictitious planewaves, will enable the direct generation of real matrices.

Another promising development for systems with inversion symmetry is the possible transformation of the mixed-product basis (MPB) functions, which serve as a basis for two-particle functions used to describe non-local quantities. A key advantage of this

transformation proposed by Betzinger and coworkers [30] concerns the computation of hybrid functionals. In analogy to the method presented in this project, this approach would yield a real-valued Coulomb matrix, ultimately speeding up the generally very computationally expensive computation of the non-local exchange potential. Beyond this, applying the same strategy to GW calculations would result in a real matrix representation of two-particle functions such as the polarizability, further enhancing computational performance [31]. These approaches illustrate the wider potential of symmetry-based optimizations, paving the way to further improve the computational efficiency of the **`exciting`** code.

7 Bibliography

[1] P. Hohenberg and W. Kohn. "Inhomogeneous Electron Gas". In: Phys. Rev. 136 (3B Nov. 1964), B864–B871. DOI: 10.1103/PhysRev.136.B864. URL: https://link.aps.org/doi/10.1103/PhysRev.136.B864.

[2] W. Kohn and L. J. Sham. "Self-Consistent Equations Including Exchange and Correlation Effects". In: Phys. Rev. 140 (4A Nov. 1965), A1133–A1138. DOI: 10.1103/PhysRev.140.A1133. URL: https://link.aps.org/doi/10.1103/PhysRev.140.A1133.

[3] Andris Gulans et al. "exciting: a full-potential all-electron package implementing density-functional theory and many-body perturbation theory". In: Journal of Physics: Condensed Matter 26.36 (Aug. 2014), p. 363202. DOI: 10.1088/0953-8984/26/36/363202. URL: https://dx.doi.org/10.1088/0953-8984/26/36/363202.

[4] Andris Gulans, Anton Kozhevnikov, and Claudia Draxl. "Microhartree precision in density functional theory calculations". In: Phys. Rev. B 97 (16 Apr. 2018), p. 161105. DOI: 10.1103/PhysRevB.97.161105. URL: https://link.aps.org/doi/10.1103/PhysRevB.97.161105.

[5] David J. Singh and Lars Nordström. Planewaves, pseudopotentials, and the LAPW method. 2006. URL: http://www.myilibrary.com?id=63435.

[6] Hyung Joon Kim et al. "Physical properties of transparent perovskite oxides (Ba,La)SnO_3 with high electrical mobility at room temperature". In: Phys. Rev. B 86 (16 Oct. 2012), p. 165205. DOI: 10.1103/PhysRevB.86.165205. URL: https://link.aps.org/doi/10.1103/PhysRevB.86.165205.

[7] Karthik Krishnaswamy et al. "First-principles analysis of electron transport in $BaSnO_3$". In: Phys. Rev. B 95 (20 May 2017), p. 205202. DOI: 10.1103/PhysRevB.95.205202. URL: https://link.aps.org/doi/10.1103/PhysRevB.95.205202.

[8] Wahib Aggoune et al. "A consistent picture of excitations in cubic BaSnO3 revealed by combining theory and experiment". In: Communications Materials 3.1 (Mar. 2022). ISSN: 2662-4443. DOI: 10.1038/s43246-022-00234-6. URL: http://dx.doi.org/10.1038/s43246-022-00234-6.

[9] M. Born and R. Oppenheimer. “Zur Quantentheorie der Molekeln”. In: Annalen der Physik 389.20 (1927), pp. 457–484. DOI: https://doi.org/10.1002/andp.19273892002. eprint: https://onlinelibrary.wiley.com/doi/pdf/10.1002/andp.19273892002. URL: https://onlinelibrary.wiley.com/doi/abs/10.1002/andp.19273892002.

[10] John P. Perdew, Kieron Burke, and Matthias Ernzerhof. “Generalized Gradient Approximation Made Simple”. In: Phys. Rev. Lett. 77 (18 Oct. 1996), pp. 3865–3868. DOI: 10.1103/PhysRevLett.77.3865. URL: https://link.aps.org/doi/10.1103/PhysRevLett.77.3865.

[11] John P. Perdew et al. “Meta-generalized gradient approximation: Explanation of a realistic nonempirical density functional”. In: The Journal of Chemical Physics 120.15 (Apr. 2004), pp. 6898–6911. ISSN: 0021-9606. DOI: 10.1063/1.1665298. eprint: https://pubs.aip.org/aip/jcp/article-pdf/120/15/6898/19201290/6898_1_online.pdf. URL: https://doi.org/10.1063/1.1665298.

[12] A. Arbuznikov. “Hybrid exchange correlation functionals and potentials: Concept elaboration”. In: Journal of Structural Chemistry 48 (Dec. 2007), S1–S31. DOI: 10.1007/s10947-007-0147-0.

[13] J. C. Slater. “Wave Functions in a Periodic Potential”. In: Phys. Rev. 51 (10 May 1937), pp. 846–851. DOI: 10.1103/PhysRev.51.846. URL: https://link.aps.org/doi/10.1103/PhysRev.51.846.

[14] O. Krogh Andersen. “Linear methods in band theory”. In: Phys. Rev. B 12 (8 Oct. 1975), pp. 3060–3083. DOI: 10.1103/PhysRevB.12.3060. URL: https://link.aps.org/doi/10.1103/PhysRevB.12.3060.

[15] D D Koelling and G O Arbman. “Use of energy derivative of the radial solution in an augmented plane wave method: application to copper”. In: Journal of Physics F: Metal Physics 5.11 (Nov. 1975), p. 2041. DOI: 10.1088/0305-4608/5/11/016. URL: https://dx.doi.org/10.1088/0305-4608/5/11/016.

[16] E Sjöstedt, L Nordström, and D.J Singh. “An alternative way of linearizing the augmented plane-wave method”. In: Solid State Communications 114.1 (2000), pp. 15–20. ISSN: 0038-1098. DOI: https://doi.org/10.1016/S0038-1098(99)00577-3. URL: https://www.sciencedirect.com/science/article/pii/S0038109899005773.

[17] David Singh. “Ground-state properties of lanthanum: Treatment of extended-core states”. In: Phys. Rev. B 43 (8 Mar. 1991), pp. 6388–6392. DOI: 10.1103/PhysRevB.43.6388. URL: https://link.aps.org/doi/10.1103/PhysRevB.43.6388.

[18] Walter Borchardt-Ott. Crystallography. eng. 1st ed. 1993. Berlin, Heidelberg, 1993. ISBN: 9783662006085.

[19] Mois I. Aroyo et al. "Bilbao Crystallographic Server. II. Representations of crystallographic point groups and space groups". In: Acta Crystallographica Section A 62.2 (Mar. 2006), pp. 115–128. DOI: 10.1107/S0108767305040286. URL: https://doi.org/10.1107/S0108767305040286.

[20] M.S. Dresselhaus, G. Dresselhaus, and A. Jorio. Group Theory: Application to the Physics of Condensed Matter. Springer Berlin Heidelberg, 2007. ISBN: 9783540328971. URL: https://books.google.de/books?id=sKaH8vrfmnQC.

[21] E.P. Wigner. Group Theory: And Its Application to the Quantum Mechanics of Atomic Spectra. Elsevier Science, 1959. ISBN: 9781483275765. URL: https://books.google.de/books?id=UITNCgAAQBAJ.

[22] Miguel A. Blanco, M. Flórez, and M. Bermejo. "Evaluation of the rotation matrices in the basis of real spherical harmonics". In: Journal of Molecular Structure: THEOCHEM 419.1 (1997), pp. 19–27. ISSN: 0166-1280. DOI: https://doi.org/10.1016/S0166-1280(97)00185-1. URL: https://www.sciencedirect.com/science/article/pii/S0166128097001851.

[23] Elisabeth Sjöstedt. "Augmented Planewaves, Developments and Applications to Magnetism". PhD thesis. Department of Physics, 2002, p. 67. ISBN: 91-554-5286-8.

[24] E. Anderson et al. LAPACK Users' Guide. Third. Philadelphia, PA: Society for Industrial and Applied Mathematics, 1999. ISBN: 0-89871-447-8 (paperback).

[25] Grégoire Allaire. Numerical linear algebra / Grégoire Allaire ; Sidi Mahmoud Kaber. eng. Texts in applied mathematics BV002476038 55. New York, NY, 2008. ISBN: 9780387341590.

[26] Rohit Chandra et al. Parallel programming in OpenMP. Morgan Kaufmann, 2001.

[27] Peter Blaha et al. "WIEN2k: An APW+lo program for calculating the properties of solids". In: The Journal of Chemical Physics 152.7 (Feb. 2020), p. 074101. ISSN: 0021-9606. DOI: 10.1063/1.5143061. eprint: https://pubs.aip.org/aip/jcp/article-pdf/doi/10.1063/1.5143061/16727313/074101_1_online.pdf. URL: https://doi.org/10.1063/1.5143061.

[28] The Elk Code. http://elk.sourceforge.net/.

[29] John P. Perdew et al. "Restoring the Density-Gradient Expansion for Exchange in Solids and Surfaces". In: Phys. Rev. Lett. 100 (13 Apr. 2008), p. 136406. DOI: 10.1103/PhysRevLett.100.136406. URL: https://link.aps.org/doi/10.1103/PhysRevLett.100.136406.

[30] Markus Betzinger, Christoph Friedrich, and Stefan Blügel. “Hybrid functionals within the all-electron FLAPW method: Implementation and applications of PBE0”. In: Phys. Rev. B 81 (19 May 2010), p. 195117. DOI: 10.1103/PhysRevB.81.195117. URL: https://link.aps.org/doi/10.1103/PhysRevB.81.195117.

[31] Christoph Friedrich et al. “Hybrid functionals and GW approximation in the FLAPW method”. In: Journal of physics. Condensed matter : an Institute of Physics journal 24 (July 2012), p. 293201. DOI: 10.1088/0953-8984/24/29/293201.

List of Figures

List of Tables

Selbstständigkeitserklärung

Ich erkläre hiermit, dass ich die vorliegende Arbeit selbstständig verfasst und noch nicht für andere Prüfungen eingereicht habe. Sämtliche Quellen einschließlich Internetquellen, die unverändert oder abgewandelt wiedergegeben werden, insbesondere Quellen für Texte, Grafiken, Tabellen, Bilder sowie die Nutzung von Künstlicher Intelligenz für die Erstellung von Texten und Abbildungen, sind als solche kenntlich gemacht. Mir ist bekannt, dass bei Verstößen gegen diese Grundsätze ein Verfahren wegen Täuschungsversuchs bzw. Täuschung eingeleitet wird.

Berlin, den 21.02.2025